RESEARCH ARTICLE OPEN ACCESS

Toward More Scalable Processes for Perovskite Solar Cells: A Comparison Between Planar and Mesoporous Architectures

Fatou Diaw Ndiaye[1,2] | Lara Perrin[1] | Maria Bernechea[2,3,4] | Lionel Flandin[1] | Emilie Planes[1]

[1]Univ. Grenoble Alpes, Univ. Savoie Mont Blanc, CNRS, Grenoble INP, LEPMI, Grenoble, France | [2]Instituto de Nanociencia y Materiales de Aragón (INMA) CSIC-Universidad de Zaragoza, Department of Chemical and Environmental Engineering, University of Zaragoza, Campus Río Ebro-Edificio I+D, C/Mariano Esquillor S/N, Zaragoza, Spain | [3]Centro de Investigación Biomédica en Red de Bioingeniería, Biomateriales y Nanomedicina, Instituto de Salud Carlos III, Zaragoza, Spain | [4]ARAID, Government of Aragon, Zaragoza, Spain

Correspondence: Emilie Planes (emilie.planes@univ-smb.fr)

ABSTRACT

Developing perovskite solar cells (PSCs) under ambient conditions remains challenging due to the material's sensitivity to oxygen and moisture. This study presents two types of PSCs fabricated entirely under ambient atmospheric conditions using different deposition techniques: spin coating and drop casting. Spin-coated cells were produced with a compact planar structure (C-PSC), while drop-cast cells utilized a mesoporous architecture (M-PSC), which not only lowers manufacturing costs but also reduces the environmental impact by limiting perovskite exposure to air during processing. Both architectures employed a $CH_3NH_3PbI_3$ perovskite layer, stabilized with either chloride anion (Cl^-) or ammonium valeric acid cation (AVA^+) additives to enhance film stability. The maturation process of fresh cells was also investigated, revealing that M-PSC devices benefited from increased photovoltaic activity postmaturation. Functional cells were achieved, with the C-PSC_Cl devices reaching nearly 13% power conversion efficiency (PCE) and M-PSC_AVAI_m devices attaining a PCE of 10.7%. The M-PSCs also showed larger active areas and more consistent performance, underscoring their reproducibility and suitability for scaling. This study provides valuable insights into cost-effective and environmentally sustainable fabrication methods for PSCs, offering promising pathways for the large-scale manufacturing and deployment of PSC technologies.

1 | Introduction

Metal halide perovskites have recently emerged as highly promising materials for developing low-cost, high-efficiency solar cells. These materials have attracted substantial attention due to their contribution to the rapid increase in the perovskite solar cell (PSC) efficiencies, which have grown from 3.8% in 2009 to over 26% in 2023 [1]. This impressive performance is attributed to a unique combination of intrinsic properties: exceptional optical and electrical properties, including high absorption efficiency, a direct band gap, and excellent charge transport capabilities [2, 3]. Additionally, perovskites demonstrated notable photoluminescence (PL) properties and high defect tolerance, making them ideal candidates photovoltaic (PV) applications [4–6].

A significant advantage of perovskite-based PVs lies in their potential for low-cost production [7–10]. Unlike traditional silicon-based solar cells, that require high-temperature and energy-intensive manufacturing processes, PSCs can be fabricated using solution-based techniques at relatively low temper-

atures [11, 12]. This flexibility enables the use of inexpensive, flexible substrates and opening up new applications, such as lightweight, flexible solar panels that can be integrated into building materials or portable electronics.

For the industrialization of perovskite PV technology, however, several critical challenges must be addressed. A primary drawback of PSCs is their relatively, as perovskite materials are prone to degradation under environmental stressors like moisture, oxygen, and UV light [13–19]. This instability poses a significant barrier to long-term performance in real-world applications. Improving the stability of PSCs remains a key area of research, with efforts focused on developing more robust perovskite compositions, protective encapsulation techniques, and stable interface materials [20–23].

Another major challenge is the complexity of the fabrication processes. High-efficiency PSCs require the deposition of multiple layers, which often must be processed in controlled, inert environments to prevent material degradation [24]. This increases manufacturing costs and complicates scalability, limiting the feasibility of large-area devices and commercial production.

To address these issues, recent advancements have been made in encapsulation techniques achieving durability of up to 3000 h at 85°C/85% RH and 1000 h under UV irradiation [25–28]. Additionally, there is a strong need for scalable fabrication processes that can operate under ambient conditions, as well as for optimized perovskite compositions and device architectures to enhance performance and stability.

The primary objective of this study is to evaluate two distinct PSC architectures—planar and mesoporous—each fabricated using different deposition techniques to assess their suitability for scalable production. Spin coating, the most conventional method for PSC fabrication [29, 30], is typically conducted in inert atmospheres to prevent degradation but is limited to small areas and nonuniform thicknesses [31, 32]. In this study, spin coating was performed under ambient conditions with specific deposition precautions, forming a compact perovskite structure (C-PSC). For comparison, drop casting, a technique with greater potential for large-scale production, was also explored to create a mesoporous structure (M-PSC), resembling the architecture of dye-sensitized solar cells.

The C-PSC devices, prepared by spin coating, adopt a typical n–i–p configuration with commonly used electrodes and charge-transporting materials, with a low-temperature carbon-based upper electrode offering a cost-effective and industrially viable alternative to traditional metal contacts [33]. Conversely, the M-PSC devices produced by drop casting follow an HTL-free architecture, with a triple-mesoporous stack of TiO_2, ZrO_2, and carbon. This structure has the advantage of eliminating HTL materials, which are often thermally unstable and sensitive to moisture and oxygen, leaving only the perovskite layer as a vulnerable component [34].

All solar cells in this study use the commonly applied $MAPbI_3$ perovskite (MA = CH_3NH_3) [35], which, while relatively easy to synthesize, is known for its instability [36]. Additives such as chloride or 5-ammonium valeric acid iodide (AVAI) have been shown to improve perovskite stability without compromising other properties. In spin-coated devices, chloride is introduced to form $MAPbI_xCl_{1-x}$ mixed-anion perovskites, enhancing film morphology, carrier diffusion length, and stability [37, 38]. For drop-cast devices, AVAI is used to form $MA_{1-x}(AVA)_xPbI_3$ mixed-cation perovskites (AVA = $HOOC(CH_2)_4NH_3$), known to significantly improve both efficiency and stability [7, 28, 39].

This study investigates these two modified $MAPbI_3$ formulations across both planar (C-PSC) and mesoporous (M-PSC) configurations. Through a detailed comparison of processing techniques, cell architectures, and additive effects, combined with extensive characterization, we aim to identify fabrication processes and device architectures that deliver high performance. Additionally, we will discuss the reasons for the failure of certain approaches, whether related to process, architecture, or materials, to provide a clear understanding of the most promising pathways for large-scale production of PSCs.

2 | Experimental Part

The fabrication of solar cells (all film depositions) and characterizations were done in air under ambient conditions (25°C, humidity levels maintained below 45% during PVK deposition, obtained if needed with the help of a TTK 171Eco dehumidifier from TROTEC).

2.1 | Chemicals and Materials

Fluorine doped tin oxide (FTO)-coated glass substrates were purchased from Ossila B.V. or Solaronix S.A. (6–9 Ω^{-2}). FTO substrates were cleaned by sonication bath in a detergent aqueous solution (Hellmanex, 1%), deionized water, acetone, and isopropanol for 10 min each and dried. They were then subjected to UV-Ozone treatment for 30 min. Solutions for compact c-TiO_2 (spin or spray coating), mesoporous m-TiO_2 (Ti-Nanoxide T600/SC or Ti-Nanoxide T165/SP), and mesoporous ZrO_2 (Zr-Nanoxide ZT/SP) were provided by Solaronix. Regioregular poly(3-hexylthiophene-2,5-diyl) (reference P3HT #4002-E) was purchased from Rieke Metals. The low-temperature compact carbon paste (DN-CP01) was from Dyenamo, and the high-temperature mesoporous carbon paste (Elcocarb B/SP) from Solaronix. The perovskite ink precursor for $MAPbI_{3-x}Cl_x$ was acquired from Ossila (reference I101, $MAI:PbCl_2$ = 3:1 in DMF). The perovskite ink precursor for $MA_{1-x}(AVA)_xPbI_3$ was acquired from Solaronix (reference 76805, $MAI:PbI_2:AVAI$ = 1:1:0.05 in GBL). Anhydrous chlorobenzene 99.8% was purchased from Sigma–Aldrich, and isopropanol 99.5% and acetone were from VWR. Ultrapure water (resistivity = 18 MΩ cm) was obtained using a Millipore Milli-Q system.

2.2 | Fabrication of Spin Coated Solar Cells (Named "C-PSC")

2.2.1 | Electron Transport Layer (ETL) Deposition

c-TiO_2 and m-TiO_2 solutions were spin coated on the cleaned FTO substrates. The conditions were set at 83 rps for 30 s. The layers

were annealed 60 min at 475°C for c-TiO$_2$, and 30 min 475°C for m-TiO$_2$, producing layers with thicknesses of respectively 65 and 450 nm. Before the deposition of the perovskite, the substrates were treated with UV-Ozone for 30 min.

2.2.2 | Perovskite Deposition (Under Air Atmosphere)

The perovskite precursors' solutions were spin coated at 17 rps for 30 s. The annealing step was 30 min at 110°C for MAPbI$_{3-x}$Cl$_x$ and 5 min at 50°C for MA$_{1-x}$(AVA)$_x$PbI$_3$. Obtained thicknesses were around 300–350 nm.

2.2.3 | Hole Transport Layer (HTL) Deposition

A 15 mg mL^{-1} solution of P3HT in chlorobenzene was spin coated on the perovskite at 25 rps for 40 s, followed by 33 rps for 30 s (thickness 45 nm).

2.2.4 | Carbon Electrode Deposition

Finally, the DN-CP01 carbon paste was deposited on the stack by Doctor Blade coating. The final sample was then annealed at 120°C under vacuum for 15 min, affording a compact carbon electrode of 15 μm. Each substrate allowed to fabricate between six and eight devices with an active area between 0.1 and 0.2 cm^2.

2.2.5 | Maturation

The fresh solar cells were eventually exposed to a posttreatment in order to achieve maximal performance. This maturation step was carried out under vacuum at 40°C for 150 h.

2.3 | Fabrication of Drop Casted Solar Cells (Named "M-PSC")

2.3.1 | Electron Transport Layer (ETL) Deposition

c-TiO$_2$ and m-TiO$_2$ solutions were deposited respectively by spray pyrolysis at 400–500°C and screen-printing on the FTO substrates, followed by a 45 min firing at 500°C. This produces layers with thicknesses of respectively 20 and 500 nm.

2.3.2 | Insulating Spacer Deposition

As the perovskite layer is deposited as a final step, an intermediate insulating layer is crucial to prevent contact between the front and back electrodes and avoid ohmic shunts. A 1 μm thick mesoporous ZrO$_2$ layer was thus deposited by screen-printing, followed by firing at 500°C.

2.3.3 | Carbon Electrode Deposition

Then, the Elcocarb B/SP carbon paste was deposited by screen-printing, followed by 30 min firing at 400°C, affording a mesoporous carbon electrode of 15 μm. Once the device was

2.3.4 | Perovskite Infiltration (Under Air Atmosphere)

Finally, 5.76 μL of the perovskite precursors' solutions were drop onto the monolithic stack using a manual micropipette. It was then allowed to infiltrate into the porous structure for 30 min in a box with the lid on. After that, the device was annealed: at 50°C for MA$_{1-x}$(AVA)$_x$PbI$_3$ and at 110°C for MAPbI$_{3-x}$Cl$_x$ in an oven for 30 min (lid on), and then it was annealed for another 60 min with the box lid off. Finally, the mask was removed. In this study, the M-PSC stacks were manufactured by Solaronix S.A. and the final perovskite deposition by drop casting was conducted in our laboratory.

2.3.5 | Maturation

The fresh solar cells were eventually exposed to a posttreatment in order to achieve maximal performance. This maturation step was carried out at 40°C and 75% relative humidity (RH) for 150 h.

2.4 | Characterization

2.4.1 | Profilometry

Layer thicknesses were estimated using an Alpha-Step D-500 (KLA) stylus profilometer after scratching the layers with a scalpel (average on three measurements).

2.4.2 | X-Ray Photoelectron Spectroscopy (XPS) and Ultraviolet Photoelectron Spectroscopy (UPS)

Perovskite film onto ITO substrates was characterized by XPS and UPS at the Advanced Microscopy Laboratory (LMA) in Zaragoza on a Kratos AXIS Ultra DLD under ultra-high vacuum (1×10^{-10} mbar) conditions. Samples were prepared by depositing the perovskite solutions onto an ITO substrate by spin coating. Subsequently, the substrate was cut into 1 × 1 cm samples to fit the dimensions of the sample holder for the measuring instrument. For XPS measurements, the samples were excited by a monochromatic Al Kα source at 1486.6 eV. The analysis of the spectra was done using CasaXPS software. The binding energies were referenced to the internal C 1s standard at 284.6 eV. UPS measurements were performed using monochromatic HeI radiation (21.2 eV). The valence band energy level (E_{vb}) was calculated as indicated in the literature [40, 41].

2.4.3 | Scanning Electron Microscopy (SEM) Observations

SEM observations were performed with a FEG ZEISS Ultra 55 microscope from CMTC in Grenoble to obtain cross-section images of the devices. For M-PSCs, this measurement was done on complete solar cells: FTO/c-TiO$_2$/m-TiO$_2$/ZrO$_2$-

perovskite/carbon. For C-PSCs, the characterization was done on half-cells: FTO/c-TiO$_2$/m-TiO$_2$/perovskite.

2.4.4 | JV Measurements

The measurements were performed under a standard AM1.5G solar simulator (Newport Oriel LSC-100, 100 mW cm^{-2}) using a BioLogic-SP300 potentiostat. The power calibration (100 mW cm^{-2}) was systematically carried out each day using a calibrated reference silicon cell with a readout meter (Oriel, Model: 91150V- Series Number: 801/0871). PV activity was analyzed by density current–voltage (J–V) curves, recorded in reverse mode with a scan going from open circuit (OC) voltage (E_{oc}) to 0 V and a scan rate of 10 mV s^{-1} (software EC-Lab 11.31). The power conversion efficiency (PCE), short-circuit current density (J_{sc}), open-circuit voltage (V_{oc}), fill factor (FF), and series resistance (R_s) were then extracted using a homemade Python script on Spyder environment. The results obtained for this characterization were verified on twelve different cells for each type of solar device.

2.4.5 | Ultraviolet–Visible (UV-Vis) Spectroscopy

UV-Vis was used for absorption measurements in the 200−1100 nm range using a Shimadzu UV-2600 spectrometer with an integrating sphere accessory. For M-PSCs, carbon layer removal was required because the opacity of this layer prevents any possible transmission of light through the entire device. This was accomplished using the adhesive scotch peeling method. For C-PSCs, the characterization was performed on FTO/c-TiO$_2$/m-TiO$_2$/perovskite half-cells. During the measurements, the beam passes through the glass, FTO, and TiO$_2$/ZrO$_2$ layers until it reaches the perovskite. This technique allows the detection of the different materials constituting the active layer of the solar cell. Optical band gaps (E_g) can be calculated using the Tauc plot method applied to absorbance data. The results obtained from this characterization were verified on three different devices for each type of solar cell.

2.4.6 | Photoluminescence (PL) Spectroscopy

PL measurements were collected over the 600−900 nm range using a Shimadzu RF-6000 spectrofluorometer with a 520 nm excitation wavelength. Two filters were used: a 575 nm low-pass in front of the excitation source and a 600 nm high pass in front of the source of emission in order to suppress any artifact coming from the spectrofluorometer. Chosen measurement conditions were a scan rate of 6000 nm min^{-1}, an excitation slit of 10 nm, and an emission slit of 20 nm. For M-PSCs, the measurements were done on full devices with carbon. For C-PSCs, the characterization was performed using FTO/c-TiO$_2$/m-TiO$_2$/perovskite half-cells (the apparatus presenting a non-reflective black background in both cases). The beam hits the side of the glass through FTO, TiO$_2$/ZrO$_2$ layers until it reaches the perovskite. The results obtained from this characterization were verified on three different devices for each type of solar cell.

2.4.7 | Photoluminescence (PL) Imaging

PL imaging mapping was carried out using a homemade device consisting of a dark chamber, two monochromatic 520 nm light-emitting diode arrays, and an overhanging camera (at 30 cm) equipped with a 650 nm high-pass filter (Edmund Optics). Image treatments were done using ImageJ software. For M-PSCs, the measurements were done on full devices with carbon. For C-PSCs, the characterization was performed using FTO/c-TiO$_2$/m-TiO$_2$/perovskite half-cells (the apparatus presenting a non-reflective black background in both cases). The results obtained from this characterization were verified on three different devices for each type of solar cell.

2.4.8 | Raman Spectroscopy

Raman spectroscopy was performed using a Senterra Raman microscope spectrometer in confocal mode. The cells were analyzed using a 532 nm monochromatic laser beam, optical lens 50x and integration time of 5 × 20 s. For M-PSC samples, the carbon layer removal was required. For C-PSC ones, the characterization was performed on FTO/c-TiO$_2$/m-TiO$_2$/perovskite half-cells. The spectra obtained are normalized to TiO$_2$ signal at 400 cm^{-1}. The results obtained from this characterization were verified on two different devices for each type of solar cell.

2.4.9 | X-Ray Diffraction (XRD) Analyses

XRDs were performed on a PANalytical X'Pert PRO MPD X-Ray diffractometer between 2θ of 8° and 50° with Cu-Kα source at the Consortium of Common Technological Means (CMTC) in Grenoble. The measurements were performed on samples without carbon layer (removal for M-PSCs or half-cell for C-PSCs). The results obtained from this characterization were verified on two different devices for each type of solar cell. Match! Software was used to identify the different phases and orientations composing the perovskite layer. Table 1 proposes an attribution from the literature of the various contributions present in the diffractograms. Generally, perovskite crystallizes in a tetragonal form with two main orientations: (110)/(220) and (200)/(400), respectively, noted $O1$ and $O2$ [42–45]. Other orientations were also noted, as indicated in the table. In addition, after an extraction of the background and peak fitting by a Gaussian curve to determine peak areas, it was possible to evaluate the relative crystallinity of the perovskite and the proportions of the different perovskite orientations using the following equations.

For perovskite crystallinity:

Relative crystallinity (%)

$$= \frac{\sum(\text{Perovskite contributions})}{\text{Integrated area} - \sum(\text{Contributions other than perovskite})} \times 100 \tag{1}$$

For orientation 1:

$$\text{Proportion}_{O1}(\%) = \frac{\sum(\text{Orientation 1})}{\sum(\text{Perovskite contributions})} \times 100 \tag{2}$$

TABLE 1 | Attribution of main XRD diffraction lines.

2θ (°)	Attribution	PVK orientation
12.6	PbI$_2$	—
14	**PVK (110)**	**Orientation 1**
20	**PVK (200)**	**Orientation 2**
23.4	PVK (121)	Other orientations
24.5	PVK (202)	Other orientations
25.3	TiO$_2$	—
25.5	PbI$_2$	—
26.4	FTO	—
26.5	Graphite	—
28.4	**PVK (220)**	**Orientation 1**
30.2	ZrO$_2$	—
30.8	PVK (123)	Other orientations
31.2	PVK (222)	Other orientations
33.7	FTO/TiO$_2$	—
35	PVK (132)	Other orientations
37.7	FTO	—
40.6	**PVK (400)**	**Orientation 2**
42.6	PVK (141)	Other orientations
43.2	PVK (134)	Other orientations
45.8	PVK (116)	Other orientations
47.7	PVK (206)	Other orientations

Abbreviations: FTO, fluorine doped tin oxide; XRD, x-ray diffraction.

For orientation 2:

$$\text{Proportion}_{O2}\ (\%) = \frac{\sum (\text{Orientation 2})}{\sum (\text{Perovskite contributions})} \times 100 \quad (3)$$

For other orientations:

$$\text{Proportion}_{\text{Others}}\ (\%) = 100 - \text{Proportion}_{O1} - \text{Proportion}_{O2} \quad (4)$$

2.4.10 | Electrochemical Impedance Spectroscopy (EIS)

EIS measurements were performed under a standard AM1.5G solar simulator (Newport Oriel LSC-100, 100 mW cm^{-2}) using a BioLogic-SP300 potentiostat (SP-300 with impedance measurement option, Biologic), with a potential variation of 30 mV and a range of frequencies between 1 MHz and 0.5 Hz. First, the measurements were made with variable illumination intensity: 0.2, 0.4, 0.6, 0.8, and 1 SUN, in OC voltage. Then, the illumination is fixed at 1 SUN (100 mW cm^{-2}) and variable voltages were applied to solar cells between 0 and 0.6 V (0.20, 0.28, 0.36, 0.44, 0.52, and 0.6 V). The Nyquist plots (Re(Z) = f(−Im(Z))) are then studied and fitted by an equivalent circuit thanks to the EC-Lab-11.31 software.

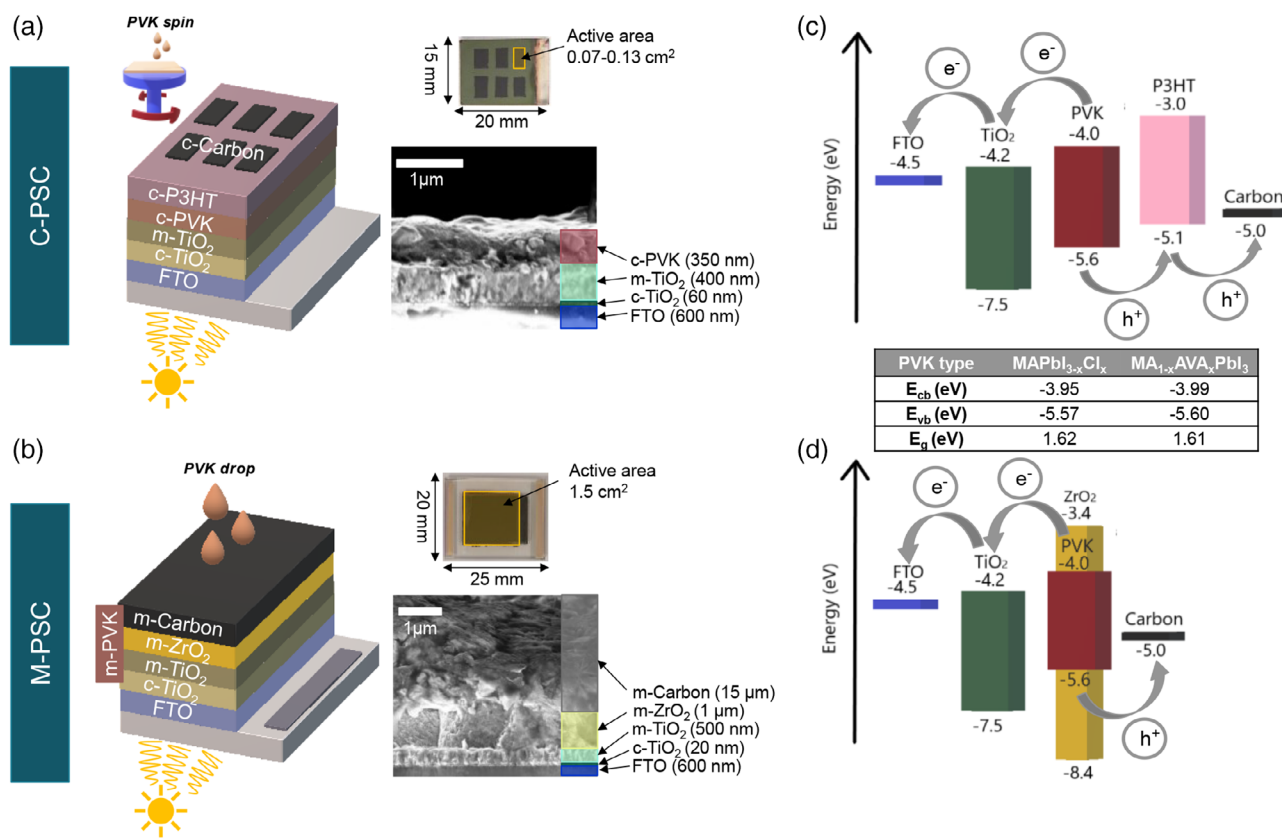## 3 | Results and Discussion

As mentioned in the introduction section, to develop air-based fabrication processes for PSCs, two types of solar cells utilizing different perovskite layer deposition methods and different architectures were studied in this article. The main features of the two types of cells are presented in Figure 1, together with the energy level diagrams of the constituting materials perfectly matching for an appropriate charge transfer.

The first type of solar cell, referred to as C-PSC in the article, was fabricated via spin coating (Figure 1a). This means that all layers of the cell were deposited using this method, except the carbon layer that was deposited via Doctor Blade coating. The C-PSC architecture follows a conventional n–i–p version: the ETL is based on a compact (c-TiO$_2$) and mesoporous (m-TiO$_2$) titanium dioxide bilayer, and the hole transport layer is P3HT. As the carbon upper electrode is deposited after perovskite, a low-temperature (100–120°C) formulation is required affording a compact carbon cathode. The proposed architecture is not the optimal in terms of performance, but it is certainly the most technically proven and arguably the least expensive [46]. The depositions were carried out on 15 × 20 mm FTO substrates, enabling the fabrication of 6 cells with active areas ranging from 0.07 to 0.13 cm^2.

The second type of solar cell, referred to as M-PSC, represents an alternative architecture to traditional solar cells [47] and was fully fabricated without using spin coating (Figure 1b). All layers can be deposited by spray coating, screen-printing, or inkjet printing, more suitable for large-scale manufacturing [48]. In this study, the perovskite layer was deposited as a final step by drop casting through a triple mesoporous scaffold. This was made possible by the use of high-temperature (400–500°C) formulations capable of producing mesoporous carbon and ZrO$_2$ layers. Used temperatures can nevertheless be qualified as relatively low compared to those required for the silicon technology. The main advantage of this technique is that the perovskite solution is very briefly exposed to the environment, reducing the risk of degradation. The architecture may appear similar to that of regular PSCs, but it differs in several key ways: the inclusion of a mesoporous spacer layer allowing both the absence of hole transporting layer and a significantly thicker perovskite layer (around 1–2 μm in M-PSCs compared to values in the 300–400 nm range for traditional PSCs) [49, 50]. The spacer layer consists in an insulating material, most of the time ZrO$_2$ which will be filled by PVK. This results in particular to the absence of possible short-circuit even after the degradation of PV devices. Thanks to the energy levels of the carbon cathode and the absence of short-circuit pathway, it is seen that hole transport to the carbon electrode can be achieved without any intermediate layer. M-PSCs are often referred to as triple-mesoporous cells, and their active surfaces are much larger than in standard PSC due the scalable processes used (1.5 cm^2 in this work). In terms of performance, M-PSCs can offer good energy conversion efficiency, although it is often lower than traditional PSCs records. However, they can compensate for this with better stability thanks to its HTL-free architecture.

The main innovation here lies in performing all depositions in an ambient air environment, in contrast with the conventional use of a glovebox [51, 52]. Both PV devices used in this study

PVK type	$MAPbI_{3-x}Cl_x$	$MA_{1-x}AVA_xPbI_3$
E_{cb} (eV)	-3.95	-3.99
E_{vb} (eV)	-5.57	-5.60
E_g (eV)	1.62	1.61

FIGURE 1 | Illustration of the two studied PV devices (a) compact C-PSC architecture fabricated using PVK spin coating and (b) mesoporous M-PSC architecture fabricated using PVK drop casting (insets show photographs of the devices with dimensions and specific surface areas, along with SEM images showing cross-sections of the devices and layers thicknesses); (b and d) energy levels diagrams and carriers flow for respectively C-PSC and M-PSC devices (exact $MAPbI_{3-x}Cl_x$ and $MA_{1-x}AVA_xPbI_3$ energy levels extracted from UPS analyses are reported in the associated table). AVA, ammonium valeric acid; PSC, perovskite solar cell; PV, photovoltaic; SEM, scanning electron microscopy; UPS, ultraviolet photoelectron spectroscopy.

also stand out for the use of carbon-based materials as cathode, which offers several advantages. Firstly, utilizing carbon can reduce manufacturing costs, as carbon-based materials are often less expensive than the metals used in traditional electrodes. Additionally, carbon-based cells can be more environmentally friendly, as they avoid the use of potentially toxic heavy metals. And finally, the carbon upper-electrode can act as a protective barrier layer to moisture stress due to its intrinsic hydrophobic nature [23, 53].

The only layer sensitive to the air environment in both PV devices here studied is the essential perovskite photo-active material. Exposed perovskite readily reacts with moisture in the air, forming hydrated crystal phases that subsequently degrade into yellow and inactive PbI_2 as a stable product [54, 55]. The performance of halide PSCs is reduced because the hydrated crystals hinder the diffusion of photo-generated carriers. To address these issues, several studies have been conducted in ambient air, employing different strategies to achieve high-quality perovskite films through spin coating. Tai et al. used $Pb(SCN)_2$ powder as an additive to incorporate thiocyanate into the crystal lattice of $MAPbI_3$, thereby improving the stability of PSCs in humid air [56]. Yan et al. used a different approach with guanabenz acetate salt to eliminate vacancies, blocking the perovskite hydration and allowing the crystallization of a high-quality film in ambient air [57].

In this study, two perovskite's formulations will be tested in both C-PSC and M-PSC described architectures. The traditional $MAPbI_3$ form will be used with two different stabilizing additives: either chloride (PSC_Cl) or AVAI (PSC_AVAI). Although $MAPbI_3$ perovskite form exhibits highly favorable properties such as excellent absorption, high carrier mobility, and relatively long carrier lifetime [37], its main drawback is its high sensitivity to environmental factors, often necessitating additives [58]. The incorporation of chloride into the perovskite structure, typically in the form of $MAPbI_{3-x}Cl_x$, has shown a beneficial effect on the material's stability [59]. Chloride ions help regulating the crystallinity and morphology of the perovskite film, thereby reducing defects and degradation induced by humidity, heat, and light [60]. It has been demonstrated in the literature that PSCs containing chloride exhibit increased durability, with better resistance to degradation under stressful environmental conditions such as heat and humidity [61]. The addition of AVAI, leading to an $MA_{1-x}(AVA)_xPbI_3$ perovskite formulation, has also demonstrated a significant improvement in solar cell efficiency [39]. This additive can promote better perovskite film morphology, thereby increasing light absorption and charge carrier separation, leading to enhanced PV conversion efficiency [7]. AVAI has also shown effectiveness in enhancing the stability of PSCs, reducing degradation phenomena caused by humidity, heat, and light, thereby prolonging the device lifetime and maintaining the performance [25]. The use of AVAI in perovskite formulation

is compatible with various fabrication processes, including film deposition techniques such as spin coating and drop casting, offering flexibility in PSC design and fabrication [47, 62].

The energy levels of our $MAPbI_{3-x}Cl_x$ and $MA_{1-x}(AVA)_xPbI_3$ perovskites are presented in the table included in Figure 1. They have been extracted from UPS measurements performed on spin-coating deposits (see Figure S1 for more precisions). Obtained values remain close and agree with those reported in the literature for similar materials [63]. This completely validates the charge transfer mechanism within both C-PSC and M-PSC devices, and hence their theoretical functioning (see Figure 1c,d), energy levels values for other layers were extracted from literature [64, 65]. XPS measurements were also performed (see Figure S2). General components of $MAPbI_3$ perovskite were detectable. For other elements originating from additives used, it seems that their amount in the final perovskite is weak enough not to alter XPS spectra. AVAI cations are introduced through AVAI reactant ($HOOC(CH_2)_4NH_3I$) in a too weak percentage to strongly modify the XPS spectra (5% of the organic cations amount). Cl anions are introduced through the introduction of $PbCl_2$ leading to a theoretically huge Cl percentage (40% of the halogen anions). However, the occurring chemical reaction is expected to release MACl easy to be sublimated during the annealing stage around 100°C [66] (halogen anions and MA being both in excess at the same level in the typical $MAI:PbCl_2 = 3:1$ formulation) [67].

Figure 2a presents the typical J–V curves obtained with our different cell configurations. One configuration is however not represented as it was found not functional. Indeed, the M-PSC_Cl configuration was not able to perform better than 0.2%–0.3%, indicating that the triple mesoporous architecture M-PSC is not compatible with $MAPbI_{3-x}Cl_x$ formulation. The typical J–V curve obtained is represented in Figure S3, together with UV-Vis and PL data. M-PSC_Cl configuration mainly produces amorphous PbI_2 as evidenced by UV-Vis spectra. The presence of $MAPbI_{3-x}Cl_x$ perovskite with probably a high Cl content could however be detected in both UV-Vis and PL spectra, with a nonoptimized band-gap close to 650 nm (instead of 765–770 nm for traditional spin-coated devices). The PL emission of these sample was relatively high and nonhomogeneous, probably related to a high quantity of defects induced by M-PSC stack architecture blocking the MACl required sublimation during the annealing stage. Additives in the perovskite formulation play a crucial role in enhancing stability and performance.

Attempts to fabricate C-PSC cells with a pure $MAPbI_3$ formulation, without any additives, did not result in functional devices [68], highlighting the very low stability of this formulation in air and the essential use of a glovebox to achieve working cells. Recent studies have shown that adding AVAI can double the performance of mesoporous carbon-based cells and greatly improve their stability [69]. The additive AVAI is generally recognized in the literature as more effective than chlorine in improving the performance and stability of $MAPbI_3$ PSCs. AVAI has been associated with significant improvements in the morphology and crystallinity of the perovskite film. For instance, Grancini et al. [70] demonstrated the long-term stability of a 5-AVAI/MAPI perovskite solar module using a 2D/3D interface engineering approach. They achieved an efficiency of 11.2% in $10 \times 10 \text{ cm}^2$

modules fabricated through a fully printable industrial process, with no degradation under AM 1.5G sunlight at 55°C for 10 000 h. Although chlorine additives can enhance cell performance, their impact appears less substantial compared to AVAI [71]. To date, one study [72] has explored the combined use of Cl and AVAI by introducing AVACl as an additive in $MAPbI_3$ cells, using $PbAc_2$ and MAI as precursors (with the acetate group potentially acting as a third additive [73]). Although the action mechanisms of AVACl and AVAI differ, the resulting efficiencies and stabilities achieved with both additives are comparable.

The three other studied configurations are functional (C-PSC_Cl, C-PSC_AVAI, and M-PSC_AVAI). Their PV parameters are presented in Figure 2 with a statistical analysis provided in Table 2. In this study, the impact of an additional posttreatment also called "maturation" was also investigated (referred as: C-PSC_Cl_m, C-PSC_AVAI_m, and M-PSC_AVAI_m). In general, for M-PSC, a maturation step is necessary after fabrication to optimize their performance. The mechanisms behind this improvement have been published recently by Farha and coworkers [27, 45]. They concluded that the maturation process in M-PSC enhances the initial PV performance without altering the device. The optimal maturation treatment depends on the cell architecture, the morphology, and the deposition method. For drop casted devices, the perovskite layer exhibited greater and more spatially varied thickness after maturation. Furthermore, they determined that this process primarily transformed the perovskite layer enhancing charge transfer. It will be thus interesting to compare the impact of such posttreatment (150 h, 40°C) on our different architectures and formulations.

As shown in Figure 2a, all cells are functional but exhibit quite different behaviors. As shown in Figure 2b, the C-PSCs performance ranges between 6.5% and 7.4%, and the highest performances are achieved for C-PSC_Cl, which have a chloride-based perovskite layer. These results are in agreement with the literature for solar cells fabricated under similar conditions. Zhang et al. developed spin-coated PCS in ambient air using carbon as the counter electrode and found that the thickness of the m-TiO_2 film greatly affects the PV performance. For samples with a m-TiO_2 thickness similar to the cells here reported (420 nm), the devices achieved 6% efficiency [74]. However, when these samples were prepared in a glovebox, the stability issues of the perovskite layer were reduced, and the performance increased, reaching efficiencies of up to 15% [51, 75]. The maturation step does not lead to an improvement in performance for any of our C-PSCs. For the M-PSCs, using AVAI as additive, the results are different. Maturation leads to a significant improvement in performance, with an increase from 7.4% to 10.2%. In summary, the M-PSC cells exhibit the best average performance. However, the C-PSC_Cl cells have a champion cell with a PCE close to 13%, whereas the highest PCE obtained for the M-PSC_AVAI cells is 10.7%. The M-PSCs nevertheless have the largest active areas and offer the most consistent performance, indicating good reproducibility of the manufacturing process.

Regarding the other PV parameters (Figure 2c and Table 2), C-PSC exhibits short-circuit current density (J_{sc}) values around 15 mA cm^{-2} and open-circuit voltages (V_{oc}) close to 0.9 V. The FF values are slightly lower for C-PSC_AVAI cells: approximately 45% compared to 55% of C-PSC_Cl cells. We will not dwell on
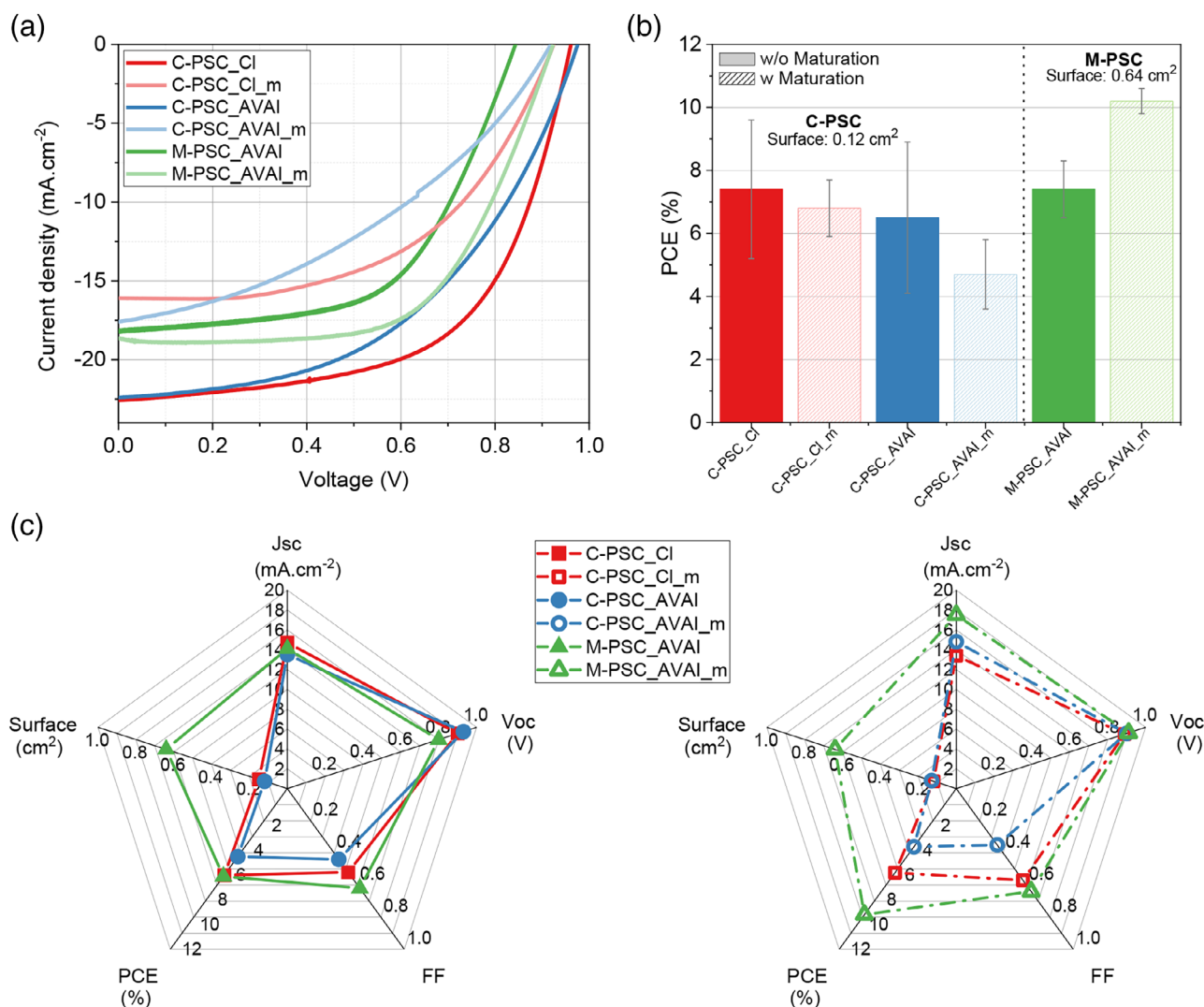
FIGURE 2 | (a) Typical J–V curves for the three functional types of photovoltaic (PV) cells before and after the maturation step; (b) power conversion efficiency (PCE) statistical values (mean and standard deviation from 12 cells of each); (c) spider chart presenting the most relevant PV parameters (mean values): PCE (%), fill factor (FF), open circuit voltage (V_{oc} [V]), short circuit current density (J_{sc} [mA cm^{-2}], together with the related photo-active measured areas).

the PV parameters after the maturation of these cells, as this treatment does not seem very effective. In comparison, the M-PSC_m cells (after maturation) exhibit slightly higher J_{sc} values, around 17.5 mA cm^{-2}, better FF values, close to 64%, and lower series resistance (R_s) values around 9 Ohm cm^2, indicating the advantage of these mesoporous architectures and thus better charge transfer within the cell. The V_{oc} values are quite similar, which can be explained by the similarity of the materials used in the three types of cells.

In drop-cast devices, defect healing occurs within the perovskite layer due to microstructural changes that enhance absorption and crystallinity [76]. The perovskite is embedded within a protective mesoporous scaffold, with the AVAI additive improving the durability of conductive pathways. Additionally, mesoporous carbon enhances nanoparticle interconnectivity, leading to better PV performance [77]. In contrast, spin-coated cells lack this mesoporous protection, making the perovskite layer thinner and more susceptible to degradation. The compact carbon layer in

these cells also limits interaction with the perovskite, reducing charge extraction efficiency and crystallinity.

In conclusion, both manufacturing processes conducted in air yield functional cells. For C-PSC cells, the performances are lower than those achieved when manufactured in a glovebox. Additionally, while the M-PSCs exhibit slightly lower performance at the initial state, their results are more reproducible across large active areas and have the potential to surpass C-PSCs after implementation of a maturation step lasting 150 h. To gain a deeper understanding of these behavioral differences, more comprehensive analyses of the perovskite layer and the complete device have been performed.

A wide range of tools and characterization methods were employed to compare the active layers of the different solar cells at different states. It should be noted that for many techniques, it is necessary to work with half-cells (cells fabricated up to the deposition of the perovskite layer) for the C-PSCs or to peel off

TABLE 2 | PV parameters of the PV cells studied before and after maturation (mean and standard deviation for 12 cells, including the results for the champion cells).

Sample		J_{sc} (mA cm^{-2})	V_{oc} (V)	FF (%)	Surface (cm^2)	R_s*Surface (Ohm cm^2)	PCE (%)
C-PSC	C-PSC_Cl	14.8 ± 3.4	0.89 ± 0.06	55.5 ± 6.6	0.12 ± 0.02	12.7 ± 7.9	7.4 ± 2.2
	Champ. device	22.6	0.96	59.3	0.07	1.2	12.9
	C-PSC_Cl_m	13.4 ± 1.7	0.89 ± 0.03	57.2 ± 4.0	0.12 ± 0.03	13.2 ± 2.8	6.8 ± 0.9
	Champ. device	16.1	0.92	53.3	0.10	3.5	7.9
	C-PSC_AVAI	15.8 ± 4.9	0.92 ± 0.08	44.2 ± 4.2	0.12 ± 0.02	14.8 ± 12.2	6.5 ± 2.4
	Champ. device	22.4	0.97	49.2	0.10	2.6	10.7
	C-PSC_AVAI_m	14.8 ± 1.7	0.90 ± 0.02	34.7 ± 4.8	0.13 ± 0.02	22.4 ± 20.2	4.7 ± 1.1
	Champ. device	17.6	0.92	38.6	0.11	10.9	6.3
M-PSC	M-PSC_AVAI	13.8 ± 1.5	0.82 ± 0.03	65.7 ± 4.7	0.64	9.0 ± 3.5	7.4 ± 0.9
	Champ. device	18.2	0.84	57.1	0.64	10.0	8.8
	M-PSC_AVAI_m	17.5 ± 0.5	0.91 ± 0.01	64.1 ± 4.6	0.64	9.4 ± 3.2	10.2 ± 0.4
	Champ. device	18.7	0.92	62.1	0.64	8.0	10.7

Abbreviations: AVAI, 5-ammonium valeric acid iodide; FF, fill factor; PCE, power conversion efficiency; PSC, perovskite solar cell; PV, photovoltaic.
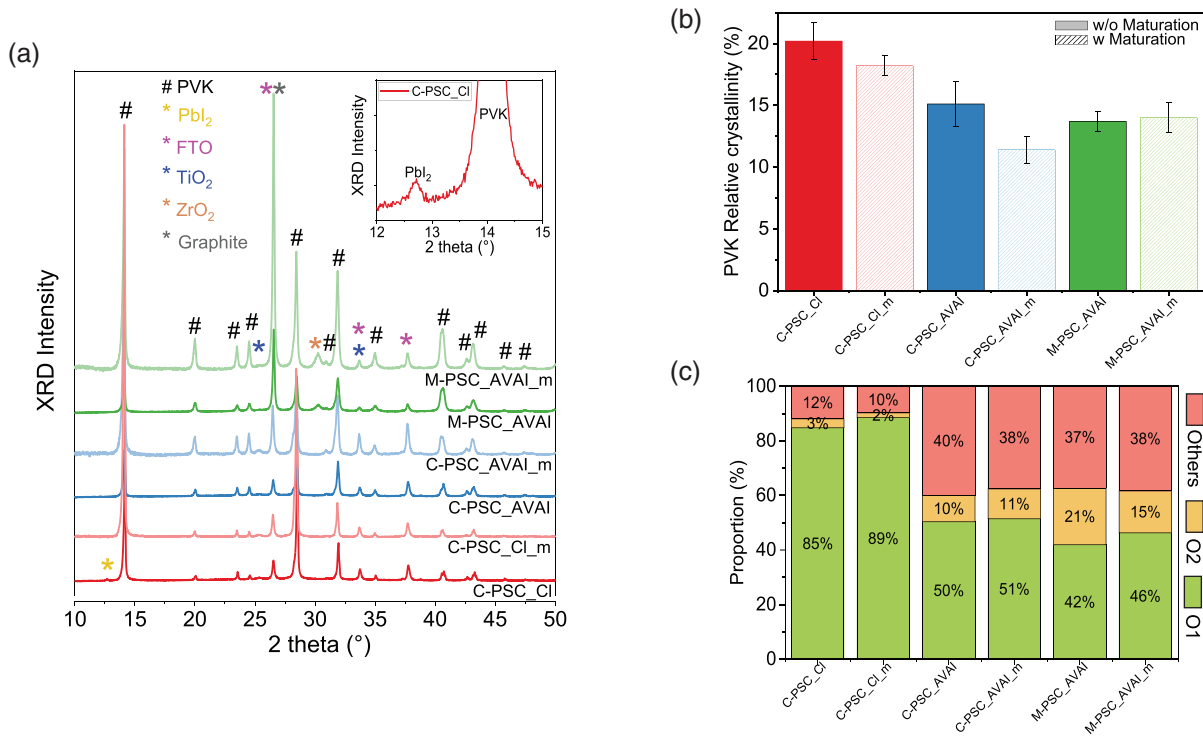
FIGURE 3 | (a) XRD patterns of perovskite layers conducted on half-cells for C-PSC and on complete cells after carbon removal for M-PSC (FTO/TiO$_2$/PVK), before and after the maturation step, with the attribution of different lines; (b) relative crystallinity (%) of perovskite (see experimental section for the definition of this parameter); (c) proportions of the two main orientations and other orientations in the perovskite (orientations are defined in the experimental section). FTO, fluorine doped tin oxide; PSC, perovskite solar cell; XRD, x-ray diffraction.

the carbon layer for the M-PSCs, to more precisely characterize the active layer.

Figure 3 shows the XRD analyses. All the layers, including the bottom of the stack (FTO, TiO$_2$, or ZrO$_2$), are detected in these thin structures. The assignment of the peaks are summarized in Table 1 (Section 2), based on literature data [42–45]. Regardless of the additive, as shown in Figure 3a, the perovskite exhibits a tetragonal structure with two major orientations: (110)/(220) at 14° and 28.4°, respectively, and (200)/(400) at 20° and 40.6°, respectively [42]. Lead iodide traces (PbI$_2$) are only detected in the C-PCS_Cl sample. The layers including AVAI as an additive show

higher intensity for peaks attributed to different orientations, named "Others": (121) at 23.4°, (202) at 24.4°, and (134) at 43.1° [45]. It is likely that AVAI impedes the perovskite crystallization, adding structural complexity. Orientations 2 contributions are also more significant in AVAI samples, and this is even slightly more pronounced in the mesoporous active layer. The mesoporous architecture of the host layer, with its high surface area and narrow structure, further hinders crystallization and favors these orientations.

A noticeable shift in the perovskite peak to lower angles is observed in spin-coated devices after the maturation process. This shift may be correlated with a reduction in the band gap, suggesting that maturation induces changes in the perovskite composition. As noted in previous research [78], this shift likely indicates a decrease in chlorine content within the perovskite. MACl is known to sublimate or degrade easily into volatile HCl and methylamine species [79], leading to atomic distortion within the perovskite structure [80]. This structural change likely also contributes to a decrease in the relative crystallinity of the spin-coated samples.

The maturation step does not lead to the formation of other products such as crystalline PbI_2, which is typically observed at 12.6° [44]. Few modifications in the patterns are visible, indicating probable microstructural modifications during this treatment. As shown in Figure 3b, it is possible to assess a relative crystallinity rate of the perovskite layer (see methodology in Section 2). The crystallinity rate for the chloride-based perovskite prepared by spin coating is close to 20%. After maturation, a decrease is observed, indicating a probable degradation of the active material. The crystallinity rate for the AVAI-based perovskites is similar regardless of the process and is lower, around 15%. There is also a decrease in this rate for the C-PSC-AVAI cells after maturation, while for the M-PSCs, this parameter increases very slightly.

The proportions of the different orientations are presented for all studied perovskites in Figure 3c. It is observed that the chloride-based perovskite is composed of over 80% of orientation 1. A very different behavior is observed for the AVAI-additive perovskite, which is composed of 50% of orientation 1, between 10% and 20% of orientation 2, and 40% of other orientations. In summary, the obtained microstructures are very different depending on the additive used, and the low impact of the process is noted in this case. It is also evident that the maturation step does not significantly alter these distributions, in agreement with previously published work within the team [45].

The absorption properties of the perovskite layer are presented in Figure 4a, allowing us to evaluate the band gap of the materials, Figure 4b. Despite the different solar cells' architecture, the analyses were conducted on slightly varied stacks (see Section 2), yet the results remain perfectly comparable. As shown in Figure 4a, all perovskite layers exhibit a main transition around 780 nm, characteristic of the 3D phase of $MAPbI_3$ perovskite. Additionally, the spectra of M-PSCs display an extra contribution around 600 nm, likely attributed to the PbI_6 octahedra of $MAPbI_3$ perovskite. This transition can redshift between 500 and 600 nm due to PVK crystal distortion [81], which is probable in the mesoporous architecture of M-PSCs. Different microstructures

in the perovskite layers between C-PSC and M-PSC cells lead to distinct absorption properties, exacerbating this transition in M-PSCs.

The absorption levels vary significantly: quite low for the C-PSC_AVAI cells and much higher for the C-PSC_Cl and M-PSC_AVAI cells. The difference in absorption between C-PSC devices can be attributed to variations in PVK crystallinity and orientation proportion. Higher crystallinity and a greater quantity of orientation 1 result in the observed higher absorption in the $MAPbI_xCl_{1-x}$ formulation compared to $MA_{1-x}(AVA)_xPbI_3$. The absorbance difference between AVAI-based C-PSC and M-PSC cells is likely due to the different PVK thicknesses (350 nm vs. 1 μm). Notably, the absorbance level of M-PSCs might be underestimated due to the carbon removal step required for this architecture.

Other transitions are observable, such as crystalline PbI_2 appearing around 500 nm for the C-PSC_Cl, in accordance with XRD data. For all perovskites, slight transitions can be distinguished between 350 and 450 nm, which, according to the literature, can be associated with a small amount of amorphous PbI_2 or minor quantities of pure chlorinated or AVAI perovskites, such as $MAPbCl_3$ or AVA_2PbI_4 [82, 83]. These phases are difficult to distinguish and were not detected by XRD.

After maturation, absorption levels differ markedly: quite low for C-PSC cells and still higher for M-PSC cells, likely due to potential degradation in C-PSC during maturation. Flat absorbance patterns suggest PVK layers with many voids or holes between crystals [9]. The ammonium valeric acid moiety, which can adsorb onto TiO_2 and ZrO_2 surfaces via its carboxylic acid group, might suppress these defects in M-PSC layers, enhancing stability compared to pure $MAPbI_3$ [28].

The perovskite layer in C-PSC_Cl cells exhibits a slightly higher band gap (∼1.62 eV) than that of AVAI-based perovskite layers (∼1.61 eV), a difference of about 5 nm, which is not significant. However, these band gap values change slightly after maturation, with a more pronounced impact on C-PSCs, particularly C-PSC_AVAI showing a decrease of over 0.2 eV (see Figure 4b). This redshift could indicate increased atomic distortion [80] due to changes in the spin-coated AVAI-based perovskite formulation during maturation, compatible with an increased AVAI insertion level in the $MAPbI_3$ lattice despite a simultaneous ∼25% decrease in crystallinity.

Raman analyses were conducted on the same samples to monitor changes in chemical functions within the perovskite layer. Initial analyses on stacks without the perovskite layer have allowed identifying specific bands for TiO_2 (143, 196, 395, and 640 cm^{-1}) and ZrO_2 (550 cm^{-1}), based on various literature sources [83, 84]. These contributions were weak when analysis was conducted on the upper part of the layer, assuming the other bands primarily pertained to the perovskite material. The band at 80 cm^{-1} is attributed to the symmetric and asymmetric breathing modes of PbI_6 octahedra [85], which can shift to higher wavenumbers in the presence of PbI_2 [86]. The band at 145 cm^{-1} is characteristic of perovskite, particularly its MA group [85], and its intensity indicates the proper formation of octahedra and full crystallinity of the perovskite.
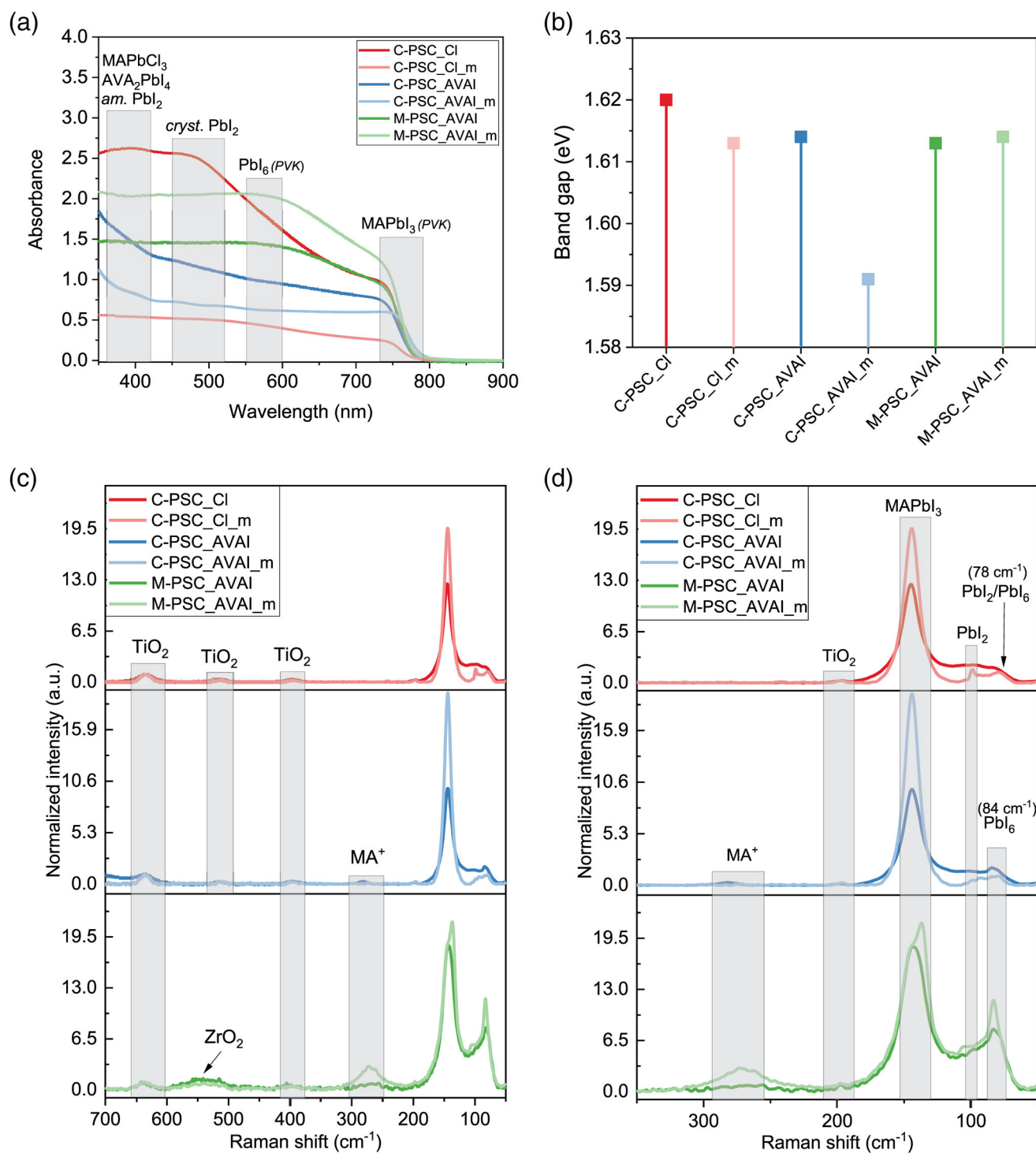
FIGURE 4 | (a) UV–visible absorbance spectra of C-PSC half-cells and of M-PSC cells after carbon removal (FTO/TiO$_2$/PVK) and (b) extracted band gap (eV) derived from Tauc-plots (see Figure S4 before and after the maturation step); (c) and (d) Raman spectra (respectively between 700–50 cm^{-1} and 350–50 cm^{-1}) performed before and after the maturation step on half-cells for C-PSC and on complete cells after carbon removal for M-PSC. FTO, fluorine doped tin oxide; PSC, perovskite solar cell.

For the chloride-based perovskite deposited by spin coating (C-PSC_Cl), the formation of the perovskite is well confirmed by the presence of bands at 78 and 145 cm^{-1}. After the maturation step, the appearance of PbI$_2$ is noted around 100 cm^{-1}, which aligns with the UV-visible absorption and XRD measurements. An increase in the intensity of the band at 145 cm^{-1} suggests a probable reorganization of the microstructure. However, since

the band at 78 cm^{-1} remains quite similar, it is challenging to fully understand the effects of these modifications.

For the AVAI-based perovskite, no formation of PbI$_2$ is observed, but an intensification of the bands at 84 and 145 cm^{-1} and the appearance of a new band at 270 cm^{-1} after the maturation step is detected. This is more pronounced for the perovskite imple-
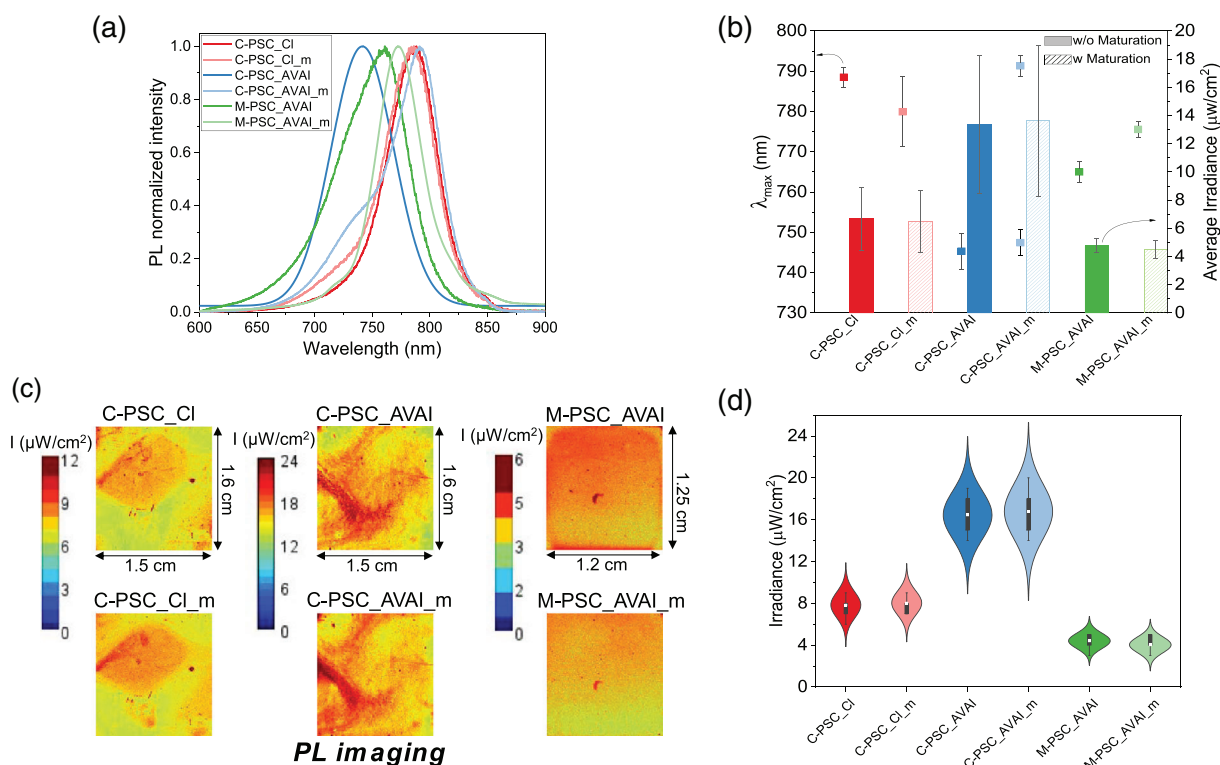
FIGURE 5 | Photoluminescence before and after maturation measured on half-cells for C-PSC (FTO/TiO$_2$/PVK) and on complete cells for M-PSC (FTO/TiO$_2$/ZrO$_2$ + PVK/C): (a) PL spectra (λ_{ex} = 520 nm); (b) (left) maximum of PL emission (extracted from PL spectra), (right) average irradiance evaluated on several solar cells (3–4 samples); (c) PL imaging photos of devices full active surface area (the color scale represents the PL emission variation); (d) statistical representation of PL images under violin plots (box plots [average, minimum, maximum, first, and third quartiles] with a kernel density plot of each side). FTO, fluorine doped tin oxide; PL, photoluminescence; PSC, perovskite solar cell.

mented by drop casting in the mesoporous structure. According to the literature, this is attributed to a better organization of the MA$^+$ cations in the periodic system and represents the second harmonic of the band at 145 cm^{-1}. Therefore, it seems that the maturation step leads to an improvement in the AVAI-based perovskite structure. This modification in the case of M-PSC-AVAI cells is clearly linked to the increase in performance observed after maturation. For the C-PSC-AVAI cells, an opposite trend is observed, with an overall decrease in performance after the maturation step. However, it seems in accordance with the absorbance redshift and crystallinity decrease antagonist behavior also observed for the latter.

To delve deeper and specifically analyze the interface effects within the cells, PL spectroscopy and imaging measurements were performed and are presented in Figure 5. Analyses were conducted from the TiO$_2$ side (the presence of the carbon layer prevented analysis from the other side). PL spectroscopy analyses are shown in Figure 5a, with the emission maxima also presented in Figure 5b (square symbols, left scale). The spectra were normalized to 1 at the maximum emission to better visualize the shifts between samples. The C-PSC_Cl cells exhibit the highest emission maximum around 790 nm, with minimal variation during the maturation step. The addition of AVAI, however, significantly decreases this parameter to 745 and 765 nm for C-PSC_AVAI and M-PSC_AVAI cells, respectively. As these shifts are more pronounced than those observed in the absorption band gaps, they are not solely related to the

PVK formulation itself but can be explained by microstructural modification induced by the additive [85, 87]. This blue shift could be related to a reduction of PVK grain size [88]. Literature also indicates a possible defect passivation in the perovskite film due to hydrogen bond formation thanks to AVAI moieties [87]. It should be noted that this phenomenon is also impacted by the layer structure, whether planar or mesoporous. Significant effects of the maturation step are observed for both cells. C-PSC-AVAI cell shows a peak splitting with a primary contribution at 790 nm and a minor one around 750 nm, close to that measured in the material before the maturation step, indicating a global redshift of the material. For the M-PSC_AVAI cell, this redshift phenomenon is also noted, though less pronounced and without peak splitting, generally explained by an improvement in the crystalline structure [89]. In the case of the mesoporous cell (M-PSC), a complete modification appears to occur, in contrast to the planar cell (C-PSC).

To complete the study, PL imaging measurements were also conducted and are presented in Figure 5c, with a statistical representation of irradiance homogeneity over a full substrate in Figure 5d (the typical discrepancy observed between several cells is also represented in Figure 5b, bar graph, right scale). At first glance, the layers of active material deposited by drop casting appear much more homogeneous compared to those obtained by spin coating. The latter seems to exhibit numerous defects, confirming that this fabrication technique may not be the most suitable for producing large-area cells. It can also be observed

that M-PSC cells show the lowest irradiance, possibly pointing the best or at least the most optimized charge recombination mechanism in these cells. Nonetheless, C-PSC_Cl cells seem to reach good performance, in agreement with PV performance (Table 2). Finally, it can be seen that the maturation step has little effect on irradiance.

To better understand the functional changes within the cells induced by maturation, we utilized EIS measurements. This widely used technique allows for the extraction of dynamic parameters within the cells. The cells were tested under two conditions: (1) at OC with varying illumination intensities, where parameters were extracted, analyzed, and plotted against the resulting open-circuit photo-potential (at this point it is worth noting that OC/V_{oc} varies with light intensity); and (2) under non-open circuit (NOC) conditions with varying DC potential (voltage) at a fixed light intensity of 1 Sun. All impedance plots are presented in Figures 6 and 8 (full graphs are experimental data and insets the model fit). By studying the complex impedance in a Nyquist diagram, a series of semicircles can be observed, each corresponding to different resistances and capacitances. The experimental data were analyzed by fitting various types of lumped circuits, which describe the different physical contributions in the system. The equivalent circuit used to fit the data was chosen from various options available in the literature. The best results with the least parameters were obtained assuming a combination of ionic and electronic conduction, as well as polarizations occurring at different interfaces.

As seen in Figures 6 and 8, the Nyquist graphs typically revealed two semicircles with different characteristic times, observed at lower and higher frequencies. The specific properties of the cells were quantified using extracted parameters (resistance and capacitance). For the M-PSC cells, the low-frequency semicircle was very small under OC conditions (Figure 6e,f) and not visible before maturation under NOC conditions (Figure 8e,f). In contrast, the C-PSC showed different behavior: only a second arc was visible under both OC and NOC conditions.

We selected a circuit with few parameters (three resistances and two capacitances) sufficient to describe the experimental results while retaining some physical relevance for the parameters (Figure 7a). Various authors suggest that changes in the five parameters of the lumped model are linked to physical alterations within the cells. The series resistor R_1 is the simplest to understand, as it represents the ohmic contributions from the contacts and wires. The model also includes two capacitances (C_1 and C_3) and two resistances (R_2 and R_3). C_1 and C_3 correspond to different aspects of the cell's behavior. C_1 reflects the bulk response of the perovskite layer and is associated with fast relaxation processes, which dominate at high frequencies (greater than 1 kHz). On the other hand, C_3 is related to slower charge movements and is noticeable at lower frequencies. Using this model, the dielectric constant of the perovskite layer (ε) can be employed to calculate the geometric capacitance of the parallel plate capacitor, given by $C_1 = \varepsilon \varepsilon_0 / d$, where d is the layer thickness and ε_0 is the permittivity of free space. C_3 is attributed to the accumulation of space charges at the interfaces. R_2 and R_3 represent resistances at different frequencies, associated with the recombination processes at the interface between the perovskite

and the extraction layers. Together, these resistances give the total recombination resistance, expressed as $R_{rec} = R_2 + R_3$.

All EIS spectra could be easily fitted using this fairly simple and physically meaningful model. The fits are presented in Figures 6 and 8 (insets). The extracted parameters are shown in Figure 7 for OC conditions and in Figure 9 for NOC conditions (see respectively Figures S5 and S6 for separate data combined in these figures). For both OC and NOC conditions, the value of C_1 is very stable even with variations in light or potential. However, significant variations are noted depending on the tested cells and few variations with maturation. For the M-PSCs measured in OC conditions, C_1 is close to 0.1 μF cm^{-2}, which is consistent with the literature, whereas for the C-PSC_Cl, C_1 is lower (around 0.01 μF cm^{-2}), see Figure 7b. This can probably be explained by a thickness effect: even though the active layer structure in M-PSCs is rather mesoporous, its thickness is around 1 μm, compared to 350 nm in planar C-PSC_Cl cells. An effect on the permittivity is likely to be noted. Almora et al. have published similar analysis for equivalent cells fabricated in glovebox [90]. Their C_1 values were 0.1 μF cm^{-2}, indicating that, in our case, air fabrication probably induces a decrease in the permittivity of the active layer. On the other hand, C-PSC_AVAI cells have very high C_1 values of around 10 μF cm^{-2}, probably indicating a poor quality of the active layer. This parameter is also very sensitive to the quality of the interfaces of the active layer with the transport layers.

C_3 is less constant with varying illumination, especially for M-PSC cells, which show an increase from 0.9 to 2.5 μF cm^{-2} from 0.2 to 1 Sun before maturation, and from 1.8 to 6 μF cm^{-2} over the same illumination range after maturation, Figure 7b. This phenomenon has been previously reported in the literature for this type of cell and is characteristic of charge carrier accumulation (mainly holes) near the TiO$_2$/PVK interface [27, 45, 91]. This effect is intensified in mesoporous structures and tends to increase with maturation. For planar structures, which are much less sensitive to this phenomenon, there is significantly less variation in this parameter with illumination.

In the EIS experiments, each semicircle can be associated with a characteristic time. Here, two times constants were defined: $\tau = R_2 C_1$ and $\tau' = R_3 C_3$, which correspond to high and low frequencies, respectively. The obtained values are presented in Figure 7c. For the first characteristic time τ, primarily associated with recombination phenomena in the active layer, the values are generally of the same order of magnitude and quite low, around 1 μs for C-PSC_Cl and M-PSC_AVAI cells. There is little effect of maturation. However, this parameter becomes very high, close to 10 ms, for C-PSC_AVAI cells, indicating very poor charge transfer in the active material. For the characteristic time τ', associated with recombination phenomena at the interfaces, all cells show similar values between 2 and 20 μs. The M-PSC cells exhibit the highest values, and there is a general increase in this parameter with maturation, indicating probable charge accumulation near the interfaces.

The recombination resistance, or charge transfer resistance, R_{rec} can be determined by simply adding the R_2 and R_3 resistances. Figure 7d presents these results as a function of V_{oc} (directly related to light intensity). For all cells, a linear relationship can be observed between R_{rec} and V_{oc} measured as a function of
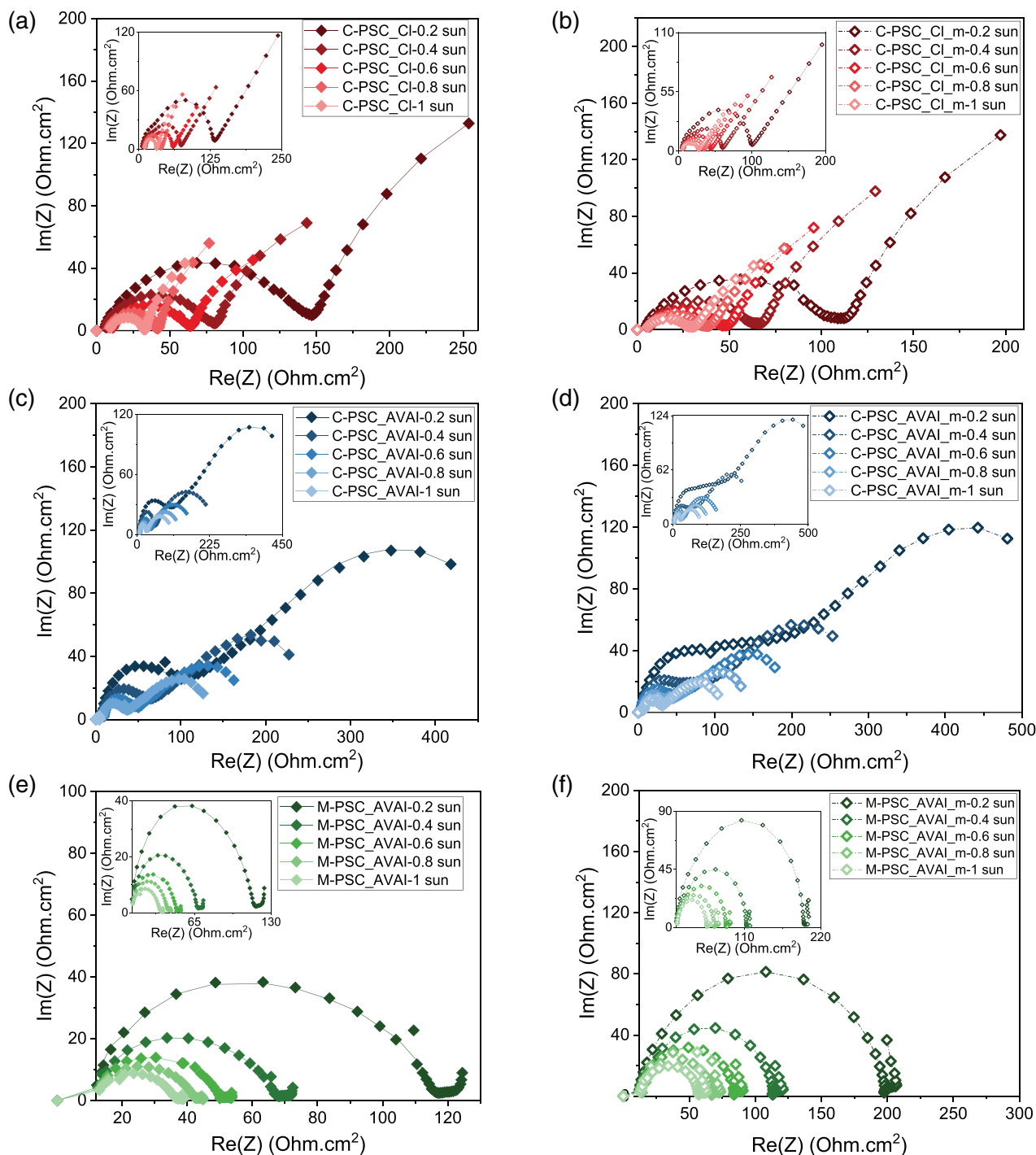
FIGURE 6 | Impedance plots (Z''–Z') measured under a voltage equal to the open circuit voltage ($V = V_{oc}$) and different illumination intensities (0.2, 0.4, 0.6, and 0.8 Sun) before and after the maturation step: (a) C-PSC_Cl; (b) C-PSC_Cl_m; (c) C-PSC_AVAI; (d) C-PSC_AVAI_m; (e) M-PSC-AVAI; (f) M-PSC-AVAI_m (full graphs are experimental data and insets the fit obtained using the model in Figure 7a). AVAI, 5-ammonium valeric acid iodide; PSC, perovskite solar cell.

the applied illumination, indicating that an ideality factor m (useful for understanding the recombination processes in solar cells) can be evaluated. The relationship between resistance and illumination can be mathematically described using an Arrhenius equation, which characterizes an activation energy [92]. This equation also enables the determination of the non-ideality coefficient m. R_{rec} can be fitted using the following expression:

$$R_{rec} = R_0 \exp\left(\frac{-qV}{mk_B T}\right)$$

where R_0 is the pre-exponential factor, q is the electron charge, V is the V_{oc} measured at a specific light intensity, m is the ideality factor, k_B is the Boltzmann constant, and T is the temperature. The absolute value of the ideality factor can help identifying the nature of the recombination mechanisms. The materials
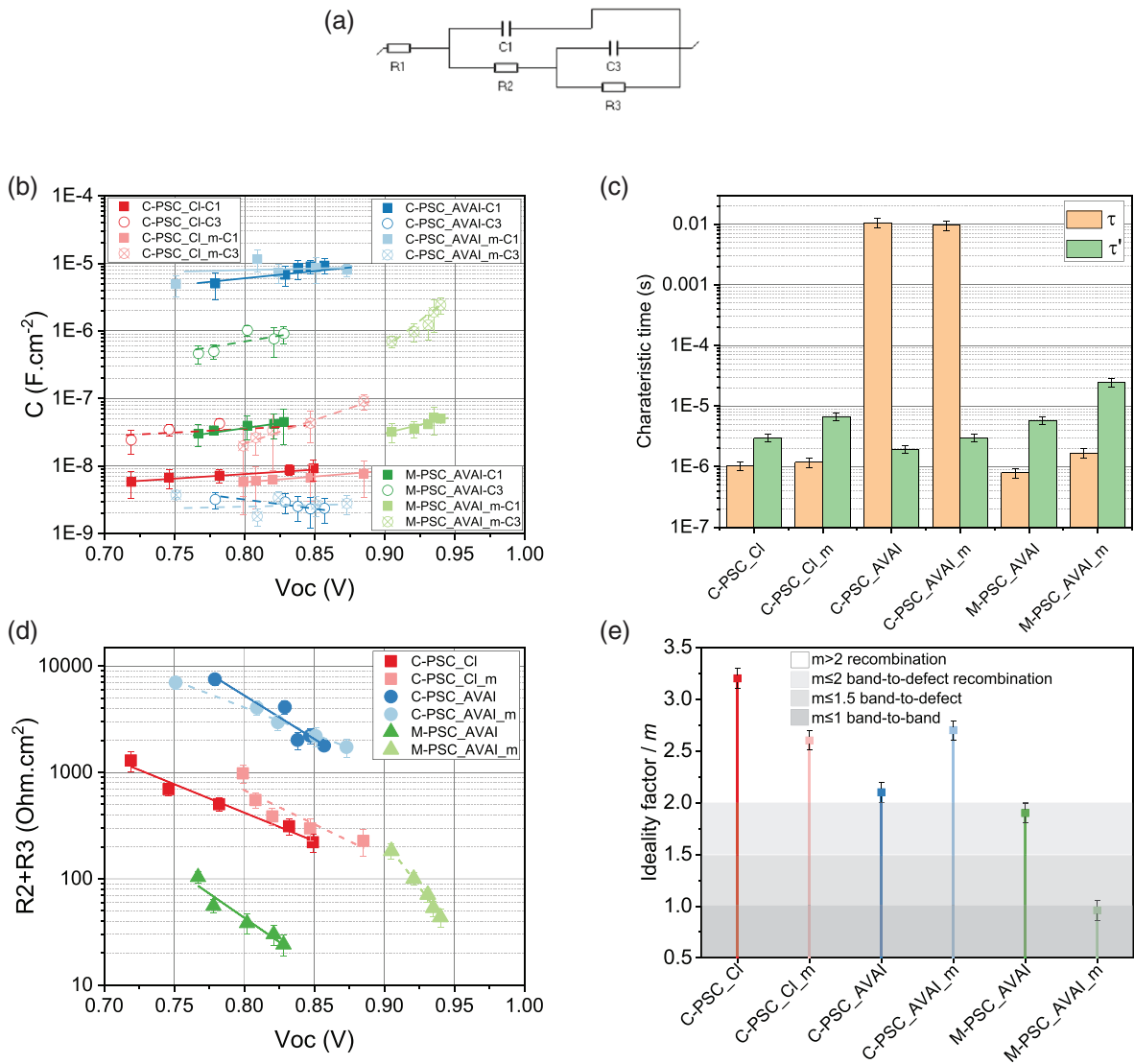
FIGURE 7 | (a) Equivalent circuit used for fitting impedance data; (b) capacitances (C_1 and C_3) and (d) recombination resistances ($R_2 + R_3$) at different light intensities (under open circuit conditions); (c) characteristic times τ and τ' and (e) ideality factors and for all solar cells before and after maturation step.

can be classified into three categories based on discrete values: $m = 1$ for band-to-band recombination, $m = 1.5$ for band-to-defect recombination within the absorber bulk, and $m = 2$ for band-to-defect recombination in the space-charge region near the surface. In summary, smaller m values indicate better cell performance closer to ideality. For planar cells, m values greater than 2 were observed, suggesting that the recombination dominant mechanism is band-to-defect recombination at the interfaces. According to the literature for similar cells fabricated under glovebox, m values between 1 and 1.5 are generally measured [93, 94], indicating the influence of fabrication process conditions on recombination and charge transfer mechanisms. C-PSC_Cl cells show a decrease in the ideality factor after maturation, while an opposite behavior is observed for C-PSC_AVAI cells. For mesoporous M-PSC cells, values below 2 are observed before maturation and around 1 after the maturation step, indicating optimal operating conditions for this type of cell.

Under NOC conditions, PV devices exhibit an exponential dependence at high DC potential, which levels off as the experiment approaches SC conditions. This suggests that PV devices are governed by the shunt resistance at a fixed light intensity and low applied bias. The transition between these two regimes occurs at voltages just below the maximum power point (MPP) of the corresponding $J(V)$ curves. At high voltage, the behavior is like that observed under OC conditions. Consequently, only the variations between 0.2 and 0.6 V are presented in Figures 8 and 9. It can be observed that the values of C_3 remain generally constant with the potential and show minimal impact from the maturation step (Figure 9a). The most significant differences are between the cells themselves, aligning with the results obtained under varying illumination. Specifically, the M-PSC_AVAI cells exhibit relatively high values around $2\,\mu F\,cm^{-2}$ before maturation, decreasing to $0.03\,\mu F\,cm^{-2}$ after maturation, indicating a probable accumulation of charge carriers at the interfaces. For cells with planar architecture, C_3 values are much lower, approximately 0.01
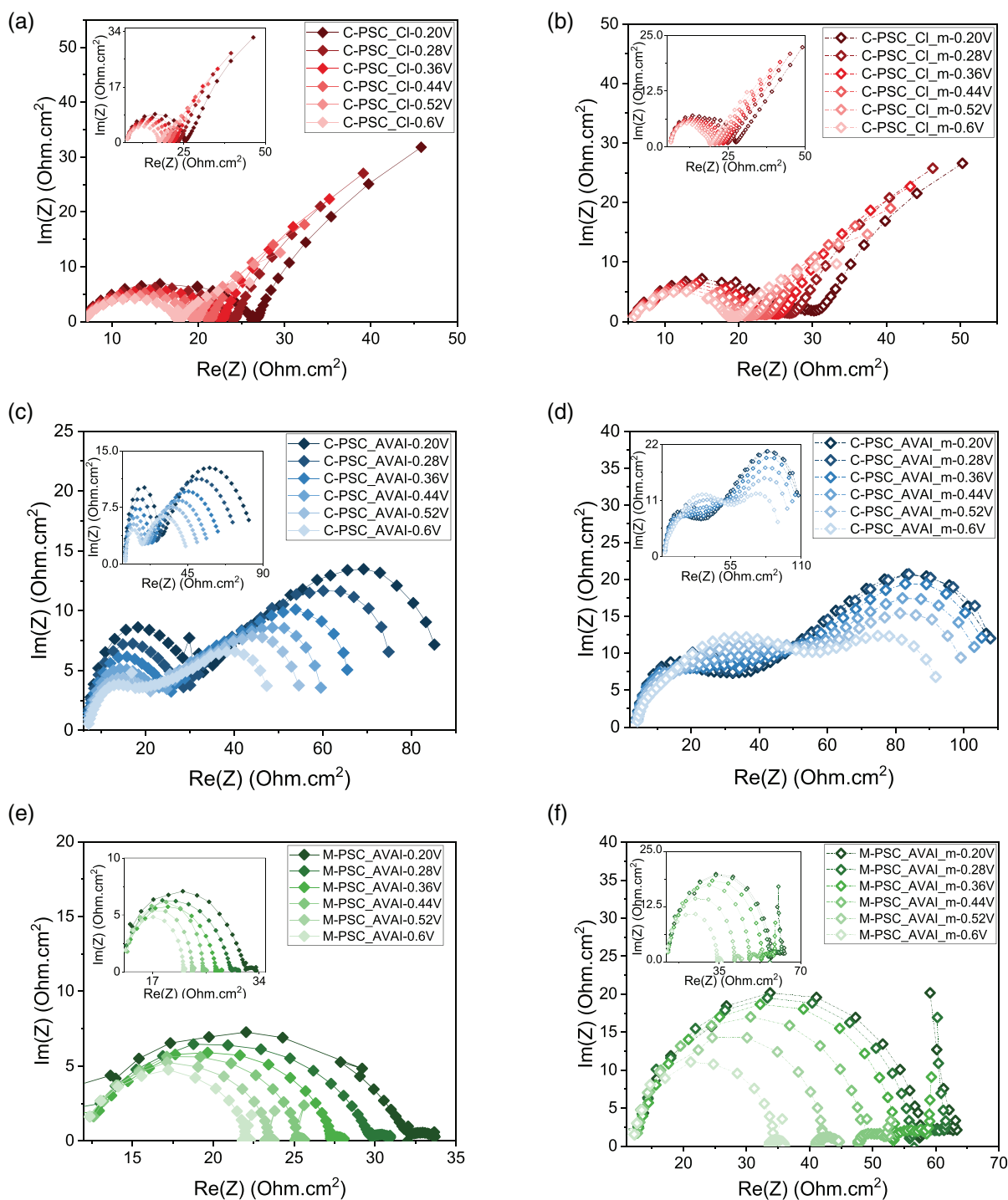
FIGURE 8 | Impedance plots (Z''–Z') measured under variable voltages for illumination of 1 Sun before and after the maturation step: (a) C-PSC_Cl; (b) C-PSC_Cl_m; (c) C-PSC_AVAI; (d) C-PSC_AVAI_m; (e) M-PSC-AVAI; (f) M-PSC-AVAI_m (full graphs are experimental data and insets the fit obtained using the model in Figure 7a). AVAI, 5-ammonium valeric acid iodide; PSC, perovskite solar cell.

and 0.005 µF cm^{-2} for C-PSC_Cl and C-PSC_AVAI cells, respectively, with little change observed after maturation, consistent with previous results.

The evolution of the recombination resistance $R_{rec} = R_2 + R_3$ as a function of V_d is shown in Figure 9b. As expected, this parameter shows little variation before the transition to higher potential. Like OC conditions, cells fabricated by spin coating exhibit much higher values, above 100 Ohm cm^2, indicating suboptimal cell

performance. In contrast, M-PSC_AVAI cells show much lower values, between 10 and 100 Ohm cm^2, confirming the effective performance of this type of device.

4 | Conclusion

In this study, we explored the development of air-based fabrication processes for PSCs by comparing two architectures—planar
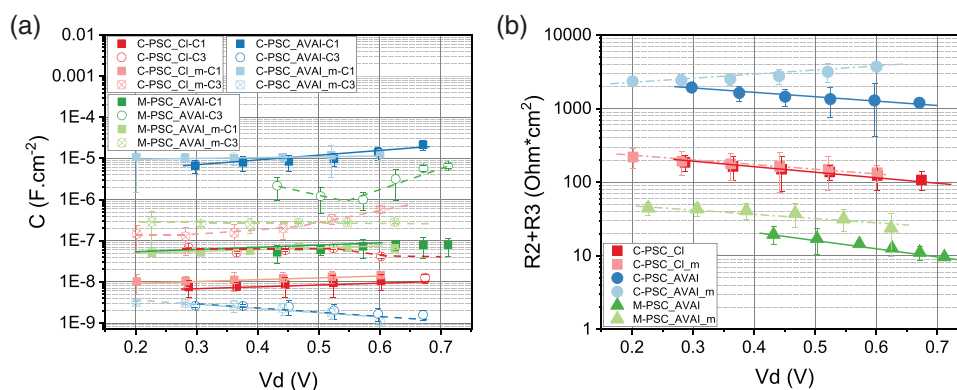
FIGURE 9 | (a) Capacitances and (b) recombination resistances under non-open (NOC) circuit conditions. Under NOC conditions, parameters are plotted versus the series corrected potential V_d = Vappl-Vseries.

(C-PSC) and mesoporous (M-PSC)—to assess their potential for industrial scalability. Our findings highlight the distinct benefits and limitations of each approach, especially regarding performance, structural stability, and suitability for large-area applications.

The planar C-PSCs, fabricated using spin coating, displayed initially higher performance, with the C-PSC_Cl devices reaching nearly 13% peak efficiency. However, the uniformity of the perovskite layer proved challenging, as the process led to thinner layers with non-uniform crystallinity and pinhole defects. These structural inconsistencies in the C-PSC samples contributed to lower device stability, with a tendency for defect formation and potential short-circuiting over time, particularly under air-based conditions. The need for glovebox processing or a controlled environment would likely remain essential for maintaining optimal device functionality in planar structures, which could be a constraint for large-scale production.

On the other hand, the M-PSCs, developed through drop casting, presented a more robust structure suitable for air-based fabrication. The mesoporous architecture, with its triple-layer scaffold, allowed thicker perovskite deposition, resulting in improved microstructural stability and greater protection against environmental degradation. Moreover, the AVAI additive enhanced both the morphology and crystallinity of the perovskite layer in M-PSCs, achieving a PCE of 10.7% initially and improving to nearly 10% after a maturation step. This thicker, well-organized structure contributed to better charge collection and reduced recombination, as indicated by the lower ideality factors postmaturation, which approached values closer to ideal band-to-band recombination mechanisms.

Impedance spectroscopy revealed distinct charge transfer dynamics in each architecture, with C-PSCs showing higher recombination losses due to structural heterogeneities. In contrast, M-PSCs exhibited a stable charge transport pathway, attributed to the mesoporous scaffold and effective additive incorporation. Despite a slightly higher charge accumulation time constant, M-PSCs showed promise for scalability, with consistent performance and structural resilience across larger surface areas.

In conclusion, while planar C-PSCs demonstrate higher initial efficiencies, their performance is less optimal for large-scale applications without a controlled environment, as they are more sensitive to air exposure. The M-PSC architecture, though showing slightly lower efficiencies, offers greater functional stability and adaptability to ambient processing, making it more suitable for industrial-scale production. This comparative study provides valuable insights into the role of architecture, deposition technique, and additives in PSC fabrication, supporting the development of robust, scalable PSC modules for commercial use.

Conflicts of Interest

The authors declare no conflicts of interest.

Data Availability Statement

The data that support the findings of this study are available from the corresponding author upon reasonable request.;

References

1. NREL, "Best Research—Cell Efficiency Chart," 06/21/2024, https://www.nrel.gov/pv/assets/pdfs/best-research-cell-efficiencies.pdf.

2. W. J. Yin, T. Shi, and Y. Yan, "Superior Photovoltaic Properties of Lead Halide Perovskites: Insights From First-Principles Theory," *Journal of Physical Chemistry C* 119, no. 10 (2015): 5253–5264, https://doi.org/10.1021/jp512077m.

3. M. A. Green, A. Ho-Baillie, and H. J. Snaith, "The Emergence of Perovskite Solar Cells," *Nature Photonics* 8, no. 7 (2014): 506–514, https://doi.org/10.1038/nphoton.2014.134.

4. L. Su, Y. Xiao, L. Lu, G. Han, and M. Zhu, "Enhanced Stability and Solar Cell Performance via π-Conjugated Lewis Base Passivation of Organic Inorganic Lead Halide Perovskites," *Organic Electronics* 77, no. 10 (2020): 9815–9821, https://doi.org/10.1016/j.orgel.2019.105519.

5. J. Y. Kim, J. W. Lee, H. S. Jung, H. Shin, and N. G. Park, "High-Efficiency Perovskite Solar Cells," *Chemical Reviews* 120, no. 15 (2020): 7867–7918, https://doi.org/10.1021/acs.chemrev.0c00107.

6. K. P. Goetz, A. D. Taylor, F. Paulus, and Y. Vaynzof, "Shining Light on the Photoluminescence Properties of Metal Halide Perovskites," *Advanced Functional Materials* 30, no. 23 (2020): 1910004, https://doi.org/10.1002/adfm.201910004.

7. A. Mei, X. Li, L. Liu, et al., "A Hole-Conductor-Free, Fully Printable Mesoscopic Perovskite Solar Cell With High Stability," *Science (1979)* 345, no. 6194 (2014): 295–298, https://doi.org/10.1126/science.1254763.

8. W. Ke, G. Fang, Q. Liu, et al., "Lowerature Solution-Processed Tin Oxide as an Alternative Electron Transporting Layer for Efficient Perovskite Solar Cells," *Journal of the American Chemical Society* 137, no. 21 (2015): 6730–6733, https://doi.org/10.1021/jacs.5b01994.

9. M. Al Katrib, L. Perrin, and E. Planes, "Optimizing Perovskite Solar Cell Architecture in Multistep Routes Including Electrodeposition," *ACS Applied Energy Materials* 5, no. 4 (2022): 4461–4474, https://doi.org/10.1021/acsaem.1c04063.

10. Z. Li, T. R. Klein, D. H. Kim, et al., "Scalable Fabrication of Perovskite Solar Cells," *Nature Reviews Materials* 3 (2018): 1–20, https://doi.org/10.1038/natrevmats.2018.17.

11. S. H. Reddy, F. Di Giacomo, and C. A. Di, "Low-Temperature-Processed Stable Perovskite Solar Cells and Modules: A Comprehensive Review," *Advanced Energy Materials* 12, no. 13 (2022): 1–37, https://doi.org/10.1002/aenm.202103534.

12. F. X. Xie, D. Zhang, H. Su, et al., "Perovskite Solar Cells With High E Ffi Ciency and Flexibility," *ACS Nano* 9, no. 1 (2015): 639–646.

13. B. Roose, K. C. Gödel, S. Pathak, et al., "Enhanced Efficiency and Stability of Perovskite Solar Cells Through Nd-Doping of Mesostructured TiO2," *Advanced Energy Materials* 6, no. 2 (2016): 1–7, https://doi.org/10.1002/aenm.201501868.

14. J. Yang, B. D. Siempelkamp, D. Liu, and T. L. Kelly, "Investigation of CH3NH3PbI3 Degradation Rates and Mechanisms in Controlled Humidity Environments Using In Situ Techniques," *ACS Nano* 9, no. 2 (2015): 1955–1963, https://doi.org/10.1021/nn506864k.

15. B. Conings, J. Drijkoningen, N. Gauquelin, et al., "Intrinsic Thermal Instability of Methylammonium Lead Trihalide Perovskite," *Advanced Energy Materials* 5, no. 15 (2015): 1–8, https://doi.org/10.1002/aenm.201500477.

16. R. Wang, M. Mujahid, Y. Duan, Z. K. Wang, J. Xue, and Y. Yang, "A Review of Perovskites Solar Cell Stability," *Advanced Functional Materials* 29, no. 47 (2019): 1–25, https://doi.org/10.1002/adfm.201808843.

17. B. Philippe, B. W. Park, R. Lindblad, et al., "Chemical and Electronic Structure Characterization of Lead Halide Perovskites and Stability Behavior Under Different Exposures – A Photoelectron Spectroscopy Investigation," *Chemistry of Materials* 27, no. 5 (2015): 1720–1731, https://doi.org/10.1021/acs.chemmater.5b00348.

18. D. Bryant, N. Aristidou, S. Pont, et al., "Light and Oxygen Induced Degradation Limits the Operational Stability of Methylammonium Lead Triiodide Perovskite Solar Cells," *Energy & Environmental Science* 9, no. 5 (2016): 1655–1660, https://doi.org/10.1039/c6ee00409a.

19. N. Aristidou, I. Sanchez-Molina, T. Chotchuangchutchaval, et al., "The Role of Oxygen in the Degradation of Methylammonium Lead Trihalide Perovskite Photoactive Layers," *Angewandte Chemie* 127, no. 28 (2015): 8326–8330, https://doi.org/10.1002/ange.201503153.

20. Z. Liu, L. Qiu, L. K. Ono, et al., "A Holistic Approach to Interface Stabilization for Efficient Perovskite Solar Modules With Over 2,000-Hour Operational Stability," *Nature Energy* 5, no. 8 (2020): 596–604, https://doi.org/10.1038/s41560-020-0653-2.

21. B. Li, Y. Li, C. Zheng, D. Gao, and W. Huang, "Advancements in the Stability of Perovskite Solar Cells: Degradation Mechanisms and Improvement Approaches," *RSC Advances* 6, no. 44 (2016): 38079–38091, https://doi.org/10.1039/c5ra27424a.

22. I. Hwang, I. Jeong, J. Lee, M. J. Ko, and K. Yong, "Enhancing Stability of Perovskite Solar Cells to Moisture by the Facile Hydrophobic Passivation," *ACS Applied Materials & Interfaces* 7, no. 31 (2015): 17330–17336, https://doi.org/10.1021/acsami.5b04490.

23. N. Kyranaki, L. Perrin, L. Flandin, et al., "Comparison of Glass–Glass Versus Glass–Backsheet Encapsulation Applied to Carbon-Based Perovskite Solar Cells," *Processes* 11, no. 9 (2023): 2742, https://doi.org/10.3390/pr11092742.

24. T. Singh and T. Miyasaka, "Stabilizing the Efficiency Beyond 20% With a Mixed Cation Perovskite Solar Cell Fabricated in Ambient Air Under Controlled Humidity," *Advanced Energy Materials* 8, no. 3 (2018): 1–9, https://doi.org/10.1002/aenm.201700677.

25. E. Kobayashi, R. Tsuji, D. Martineau, A. Hinsch, and S. Ito, "Light-Induced Performance Increase of Carbon-Based Perovskite Solar Module for 20-Year Stability," *Cell Reports Physical Science* 2, no. 12 (2021): 100648, https://doi.org/10.1016/j.xcrp.2021.100648.

26. S. W. Lee, S. Kim, S. Bae, et al., "UV Degradation and Recovery of Perovskite Solar Cells," *Scientific Reports* 6, no. November (2016): 1–10, https://doi.org/10.1038/srep38150.

27. E. Planes, C. Farha, G. D. E. Moor, S. Narbey, L. Flandin, and L. Perrin, "Interface Effects on the Stability of Carbon-Electrode-Based Perovskite Solar Cells During Damp Heating," *Advanced Materials Interfaces* 11, no. 7 (2024): 2300849, https://doi.org/10.1002/admi.202300849.

28. L. Perrin, E. Planes, T. Shioki, et al., "How Ammonium Valeric Acid Iodide Additive Can Lead to More Efficient and Stable Carbon-Based Perovskite Solar Cells: Role of Microstructure and Interfaces," *Solar RRL* 8, no. 17 (2024): 2400393, https://doi.org/10.1002/solr.202400393.

29. G. Wang, D. Liu, J. Xiang, et al., "Efficient Perovskite Solar Cell Fabricated in Ambient Air Using One-Step Spin-Coating," *RSC Advances* 6, no. 49 (2016): 43299–43303, https://doi.org/10.1039/c6ra05893k.

30. Z. Xiao, C. Bi, Y. Shao, et al., "Efficient, High Yield Perovskite Photovoltaic Devices Grown by Interdiffusion of Solution-Processed Precursor Stacking Layers," *Energy & Environmental Science* 7, no. 8 (2014): 2619–2623, https://doi.org/10.1039/c4ee01138d.

31. M. Yang, Z. Li, M. O. Reese, et al., "Perovskite Ink With Wide Processing Window for Scalable High-Efficiency Solar Cells," *Nature Energy* 2, no. 5 (2017): 1–9, https://doi.org/10.1038/nenergy.2017.38.

32. S. Razza, S. Castro-Hermosa, A. Di Carlo, and T. M. Brown, "Research Update: Large-Area Deposition, Coating, Printing, and Processing Techniques for the Upscaling of Perovskite Solar Cell Technology," *APL Materials* 4, no. 9 (2016): 091508, https://doi.org/10.1063/1.4962478.

33. D. Bogachuk, S. Zouhair, K. Wojciechowski, et al., "Low-Temperature Carbon-Based Electrodes in Perovskite Solar Cells," *Energy & Environmental Science* 13, no. 11 (2020): 3880–3916, https://doi.org/10.1039/d0ee02175j.

34. H. Chen and S. Yang, "Carbon-Based Perovskite Solar Cells Without Hole Transport Materials: The Front Runner to the Market?" *Advanced Materials* 29, no. 24 (2017): 1603994, https://doi.org/10.1002/adma.201603994.

35. T. Baikie, Y. Fang, J. M. Kadro, et al., "Synthesis and Crystal Chemistry of the Hybrid Perovskite (CH 3NH3)PbI3 for Solid-State Sensitised Solar Cell Applications," *Journal of Materials Chemistry A* 1, no. 18 (2013): 5628–5641, https://doi.org/10.1039/c3ta10518k.

36. E. Smecca, Y. Numata, I. Deretzis, et al., "Stability of Solution-Processed MAPbI3 and FAPbI3 Layers," *Physical Chemistry Chemical Physics* 18, no. 19 (2016): 13413–13422, https://doi.org/10.1039/c6cp00721j.

37. J. Zhang, K. Wang, Q. Yao, et al., "Carrier Diffusion and Recombination Anisotropy in the MAPbI3 Single Crystal," *ACS Applied Materials & Interfaces* 13, no. 25 (2021): 29827–29834, https://doi.org/10.1021/acsami.1c07056.

38. T. Zhang, M. Yang, Y. Zhao, and K. Zhu, "Controllable Sequential Deposition of Planar CH3NH3PbI3 Perovskite Films via Adjustable

Volume Expansion," *Nano Letters* 15, no. 6 (2015): 3959–3963, https://doi.org/10.1021/acs.nanolett.5b00843.

39. A. Mei, Y. Sheng, Y. Ming, et al., "Stabilizing Perovskite Solar Cells to IEC61215:2016 Standards With Over 9,000-h Operational Tracking," *Joule* 4, no. 12 (2020): 2646–2660, https://doi.org/10.1016/j.joule.2020.09.010.

40. L. Givalou, E. Christopoulos, M. K. Arfanis, et al., "ETL/Perovskite Interface Engineering Using Cadmium and Lead Chalcogenide Quantum Dots," *Electrochimica Acta* 473 (2024): 143523, https://doi.org/10.1016/j.electacta.2023.143523.

41. F. K. Chang, Y. C. Huang, J. S. Jeng, and J. S. Chen, "Band Offset of Vanadium-Doped Molybdenum Oxide Hole Transport Layer in Organic Photovoltaics," *Solid State Electronics* 122 (2016): 18–22, https://doi.org/10.1016/j.sse.2016.04.014.

42. R. Urzúa-Leiva, A. Narymany Shandy, H. Xie, M. Lira-Cantú, and G. Cárdenas-Jirón, "Effects of the Methylammonium Ion Substitution by 5-Ammoniumvaleric Acid in Lead Trihalide Perovskite Solar Cells: A Combined Experimental and Theoretical Investigation," *New Journal of Chemistry* 44, no. 34 (2020): 14642–14649, https://doi.org/10.1039/d0nj02748k.

43. A. Karavioti, E. Vitoratos, and E. Stathatos, "Improved Performance and Stability of Hole-Conductor-Free Mesoporous Perovskite Solar Cell With New Amino-Acid Iodide Cations," *Journal of Materials Science: Materials in Electronics* 31, no. 8 (2020): 6109–6117, https://doi.org/10.1007/s10854-020-03164-6.

44. Z. Ma, D. Huang, Q. Liu, et al., "Excess PbI2 Evolution for Triple-Cation Based Perovskite Solar Cells With 21.9% Efficiency," *Journal of Energy Chemistry* 66 (2022): 152–160, https://doi.org/10.1016/j.jechem.2021.07.030.

45. E. Planes, C. Farha, G. De Moor, S. Narbey, L. Perrin, and L. Flandin, "Maturing Effects in Carbon-Based Perovskite Solar Cells: Understanding and Consequences on Photovoltaic Performances," *Solar RRL* 7, no. 23 (2023): 2–5, https://doi.org/10.1002/solr.202300492.

46. Q. Q. Chu, B. Ding, J. Peng, et al., "Highly Stable Carbon-Based Perovskite Solar Cell With a Record Efficiency of Over 18% via Hole Transport Engineering," *Journal of Materials Science and Technology* 35, no. 6 (2019): 987–993, https://doi.org/10.1016/j.jmst.2018.12.025.

47. S. G. Hashmi, D. Martineau, X. Li, et al., "Air Processed Inkjet Infiltrated Carbon Based Printed Perovskite Solar Cells With High Stability and Reproducibility," *Advanced Materials Technologies* 2, no. 1 (2017): 4–9, https://doi.org/10.1002/admt.201600183.

48. S. G. Hashmi, D. Martineau, M. I. Dar, et al., "High Performance Carbon-Based Printed Perovskite Solar Cells With Humidity Assisted Thermal Treatment," *Journal of Materials Chemistry A* 5, no. 24 (2017): 12060–12067, https://doi.org/10.1039/c7ta04132b.

49. A. Priyadarshi, A. Bashir, J. T. Gunawan, et al., "Simplified Architecture of a Fully Printable Perovskite Solar Cell Using a Thick Zirconia Layer," *Energy Technology* 5, no. 10 (2017): 1866–1872, https://doi.org/10.1002/ente.201700474.

50. C. Momblona, O. Malinkiewicz, C. Roldán-Carmona, et al., "Efficient Methylammonium Lead Iodide Perovskite Solar Cells With Active Layers From 300 to 900 Nm," *APL Materials* 2, no. 8 (2014): 081504, https://doi.org/10.1063/1.4890056.

51. S. Zouhair, S. M. Yoo, D. Bogachuk, et al., "Employing 2D-Perovskite as an Electron Blocking Layer in Highly Efficient (18.5%) Perovskite Solar Cells With Printable Low Temperature Carbon Electrode," *Advanced Energy Materials* 12, no. 21 (2022): 1–10, https://doi.org/10.1002/aenm.202200837.

52. H. Zhang, J. Xiao, J. Shi, et al., "Self-Adhesive Macroporous Carbon Electrodes for Efficient and Stable Perovskite Solar Cells," *Advanced Functional Materials* 28, no. 39 (2018): 1–8, https://doi.org/10.1002/adfm.201802985.

53. M. Hadadian, J. H. Smått, and J. P. Correa-Baena, "The Role of Carbon-Based Materials in Enhancing the Stability of Perovskite Solar Cells,"

Energy & Environmental Science 13, no. 5 (2020): 1377–1407, https://doi.org/10.1039/c9ee04030g.

54. J. Zhao, B. Cai, Z. Luo, et al., "Investigation of the Hydrolysis of Perovskite Organometallic Halide CH3NH3PbI3 in Humidity Environment," *Scientific Reports* 6 (2016): 1–6, https://doi.org/10.1038/srep21976.

55. A. M. A. Leguy, Y. Hu, M. Campoy-Quiles, et al., "Reversible Hydration of CH3NH3PbI3 in Films, Single Crystals, and Solar Cells," *Chemistry of Materials* 27, no. 9 (2015): 3397–3407, https://doi.org/10.1021/acs.chemmater.5b00660.

56. Q. Tai, P. You, H. Sang, et al., "Efficient and Stable Perovskite Solar Cells Prepared in Ambient Air Irrespective of the Humidity," *Nature Communications* 7 (2016): 1–8, https://doi.org/10.1038/ncomms11105.

57. L. Yan, H. Huang, P. Cui, et al., "Fabrication of Perovskite Solar Cells in Ambient Air by Blocking Perovskite Hydration With Guanabenz Acetate Salt," *Nature Energy* 8, no. 10 (2023): 1158–1167, https://doi.org/10.1038/s41560-023-01358-w.

58. J. Hieulle, X. Wang, C. Stecker, et al., "Unraveling the Impact of Halide Mixing on Perovskite Stability," *Journal of the American Chemical Society* 141, no. 8 (2019): 3515–3523, https://doi.org/10.1021/jacs.8b11210.

59. H. Yu, F. Wang, F. Xie, W. Li, J. Chen, and N. Zhao, "The Role of Chlorine in the Formation Process of "CH3NH3PbI3-xClx" Perovskite," *Advanced Functional Materials* 24, no. 45 (2014): 7102–7108, https://doi.org/10.1002/adfm.201401872.

60. C. Quarti, E. Mosconi, P. Umari, and F. De Angelis, "Chlorine Incorporation in the CH3NH3PbI3 Perovskite: Small Concentration, Big Effect," *Inorganic Chemistry* 56, no. 1 (2017): 74–83, https://doi.org/10.1021/acs.inorgchem.6b01681.

61. J. Chae, Q. Dong, J. Huang, and A. Centrone, "Chloride Incorporation Process in CH3NH3PbI3-xClx Perovskites via Nanoscale Bandgap Maps," *Nano Letters* 15, no. 12 (2015): 8114–8121, https://doi.org/10.1021/acs.nanolett.5b03556.

62. N. Wei, Y. Chen, Y. Miao, et al., "5-Ammonium Valeric Acid Iodide to Stabilize MAPbI3via a Mixed-Cation Perovskite With Reduced Dimension," *Journal of Physical Chemistry Letters* 11, no. 19 (2020): 8170–8176, https://doi.org/10.1021/acs.jpclett.0c02528.

63. V. Zardetto, B. L. Williams, A. Perrotta, et al., "Atomic Layer Deposition for Perovskite Solar Cells: Research Status, Opportunities and Challenges," *Sustain Energy Fuels* 1, no. 1 (2017): 30–55, https://doi.org/10.1039/c6se00076b.

64. Q. Wang, S. Liu, Y. Ming, et al., "Improvements in Printable Mesoscopic Perovskite Solar Cells: Via Thinner Spacer Layers," *Sustain Energy Fuels* 2, no. 11 (2018): 2412–2418, https://doi.org/10.1039/c8se00332g.

65. Y. Xiong, Y. Liu, K. Lan, et al., "Fully Printable Hole-Conductor-Free Mesoscopic Perovskite Solar Cells Based on Mesoporous Anatase Single Crystals," *New Journal of Chemistry* 42, no. 4 (2018): 2669–2674, https://doi.org/10.1039/c7nj04448h.

66. K. H. Stone, A. Gold-Parker, V. L. Pool, et al., "Transformation From Crystalline Precursor to Perovskite in PbCl2-Derived MAPbI3," *Nature Communications* 9, no. 1 (2018), https://doi.org/10.1038/s41467-018-05937-4.

67. M. Spalla, E. Planes, L. Perrin, M. Matheron, S. Berson, and L. Flandin, "Alternative Electron Transport Layer Based on Al-Doped ZnO and SnO2 for Perovskite Solar Cells: Impact on Microstructure and Stability," *ACS Applied Energy Materials* 2, no. 10 (2019): 7183–7195, https://doi.org/10.1021/acsaem.9b01160.

68. M. Spalla, L. Perrin, E. Planès, M. Matheron, S. Berson, and L. Flandin, "Influence of Chloride/Iodide Ratio in MAPbI3-xClx Perovskite Solar Devices: Case of Low Temperature Processable AZO Sub-Layer," *Energies (Basel)* 13, no. 8 (2020): 1927.

69. E. Planes, C. Farha, G. D. E. Moor, S. Narbey, L. Flandin, and L. Perrin, "Interface Effects on the Stability of Carbon-Electrode-Based Perovskite

Solar Cells During Damp Heating," *Advanced Materials Interfaces* 11, no. 7 (2024): 2300849, https://doi.org/10.1002/admi.202300849.

70. G. Grancini, C. Roldán-Carmona, I. Zimmermann, et al., "One-Year Stable Perovskite Solar Cells by 2D/3D Interface Engineering," *Nature Communications* 8 (2017): 1–8, https://doi.org/10.1038/ncomms15684.

71. L. Zhou, Y. Zuo, T. K. Mallick, and S. Sundaram, "Enhanced Efficiency of Carbon-Based Mesoscopic Perovskite Solar Cells Through a Tungsten Oxide Nanoparticle Additive in the Carbon Electrode," *Scientific Reports* 9, no. 1 (2019): 8778, https://doi.org/10.1038/s41598-019-45374-x.

72. Y. Li, P. J. Lohr, A. Segapeli, et al., "Influence of Halides on the Interactions of Ammonium Acids With Metal Halide Perovskites," *ACS Applied Materials & Interfaces* 15, no. 20 (2023): 24387–24398, https://doi.org/10.1021/acsami.3c01432.

73. Y. Xiao, L. Yang, G. Han, Y. Li, M. Li, and H. Li, "Effects of Methylammonium Acetate on the Perovskite Film Quality for the Perovskite Solar Cell," *Organic Electronics* 65 (2019): 201–206, https://doi.org/10.1016/j.orgel.2018.11.020.

74. F. Zhang, X. Yang, H. Wang, M. Cheng, J. Zhao, and L. Sun, "Structure Engineering of Hole-Conductor Free Perovskite-Based Solar Cells With Low-Temperature-Processed Commercial Carbon Paste as Cathode," *ACS Applied Materials & Interfaces* 6, no. 18 (2014): 16140–16146, https://doi.org/10.1021/am504175x.

75. S. K. K. Aung, A. Vijayan, T. Seetawan, and G. Boschloo, "Improved Efficiency of Perovskite Solar Cells With Low-Temperature-Processed Carbon by Introduction of a Doping-Free Polymeric Hole Conductor," *Solar RRL* 6, no. 8 (2022): 2100773, https://doi.org/10.1002/solr.202100773.

76. L. Wagner, L. E. Mundt, G. Mathiazhagan, et al., "Distinguishing Crystallization Stages and Their Influence on Quantum Efficiency During Perovskite Solar Cell Formation in Real-Time," *Scientific Reports* 7, no. 1 (2017): 14899, https://doi.org/10.1038/s41598-017-13855-6.

77. A. Pockett, D. Raptis, S. M. P. Meroni, J. Baker, T. Watson, and M. Carnie, "Origin of Exceptionally Slow Light Soaking Effect in Mesoporous Carbon Perovskite Solar Cells With AVA Additive," *The Journal of Physical Chemistry C* 123, no. 18 (2019): 11414–11421, https://doi.org/10.1021/acs.jpcc.9b01058.

78. M. Al Katrib, E. Planes, and L. Perrin, "Effect of Chlorine Addition on the Performance and Stability of Electrodeposited Mixed Perovskite Solar Cells," *Chemistry of Materials* 34, no. 5 (2022): 2218–2230, https://doi.org/10.1021/acs.chemmater.1c04021.

79. S. T. Williams, F. Zuo, C. C. Chueh, C. Y. Liao, P. W. Liang, and A. K. Y. Jen, "Role of Chloride in the Morphological Evolution of Organo-Lead Halide Perovskite Thin Films," *ACS Nano* 8, no. 10 (2014): 10640–10654, https://doi.org/10.1021/nn5041922.

80. G. Liu, L. Kong, P. Guo, et al., "Two Regimes of Bandgap Red Shift and Partial Ambient Retention in Pressure-Treated Two-Dimensional Perovskites," *ACS Energy Letters* 2, no. 11 (2017): 2518–2524, https://doi.org/10.1021/acsenergylett.7b00807.

81. S. M. Mousavi, M. Alidaei, F. Arabpour Roghabadi, V. Ahmadi, S. M. Sadrameli, and J. Vapaavuori, "Stability Improvement of MAPbI3-Based Perovskite Solar Cells Using a Photoactive Solid-Solid Phase Change Material," *Journal of Alloys and Compounds* 897 (2022): 163142, https://doi.org/10.1016/j.jallcom.2021.163142.

82. M. Spalla, L. Perrin, E. Planès, M. Matheron, S. Berson, and L. Flandin, "Influence of Chloride/Iodide Ratio in MAPBI3-xClx Perovskite Solar Devices: Case of Low Temperature Processable Azo Sub-Layer," *Energies (Basel)* 13, no. 8 (2020): 1927, https://doi.org/10.3390/en13081927.

83. M. Lubas, J. J. Jasinski, M. Sitarz, L. Kurpaska, P. Podsiad, and J. Jasinski, "Raman Spectroscopy of TiO2 Thin Films Formed by Hybrid Treatment for Biomedical Applications," *Spectrochimica Acta, Part A: Molecular and Biomolecular Spectroscopy* 133 (2014): 867–871, https://doi.org/10.1016/j.saa.2014.05.045.

84. T. Hirata and F. S. Ohuchi, "Temperature Dependence of the Raman Spectra of 1T-TaS2," *Solid State Communications* 117, no. 6 (2001): 361–364, https://doi.org/10.1016/S0038-1098(00)00468-3.

85. S. M. Jain, B. Philippe, E. M. J. Johansson, et al., "Vapor Phase Conversion of PbI2 to CH3NH3PbI3: Spectroscopic Evidence for Formation of an Intermediate Phase," *Journal of Materials Chemistry A Materials* 4, no. 7 (2016): 2630–2642, https://doi.org/10.1039/c5ta08745g.

86. K. E. A. Hooper, H. K. H. Lee, M. J. Newman, et al., "Probing the Degradation and Homogeneity of Embedded Perovskite Semiconducting Layers in Photovoltaic Devices by Raman Spectroscopy," *Physical Chemistry Chemical Physics* 19, no. 7 (2017): 5246–5253, https://doi.org/10.1039/c6cp05123e.

87. K. Fan, K. Dai, J. Wang, et al., "Enhanced Mechanical Stability of Perovskite Film by Modulating the Toughness of Grain Boundary," *Organic Electronics* 117 (2023): 106778, https://doi.org/10.1016/j.orgel.2023.106778.

88. A. Ummadisingu, S. Meloni, A. Mattoni, W. Tress, and M. Grätzel, "Crystal-Size-Induced Band Gap Tuning in Perovskite Films," *Angewandte Chemie – International Edition* 60, no. 39 (2021): 21368–21376, https://doi.org/10.1002/anie.202106394.

89. M. E. Kayesh, K. Matsuishi, R. Kaneko, et al., "Coadditive Engineering With 5-Ammonium Valeric Acid Iodide for Efficient and Stable Sn Perovskite Solar Cells," *ACS Energy Letters* 4, no. 1 (2019): 278–284, https://doi.org/10.1021/acsenergylett.8b02216.

90. O. Almora, P. López-Varo, R. Escalante, et al. Degradation Analysis of Perovskite Solar Cells via Short-Circuit Impedance Spectroscopy: A Case Study on NiOx Passivation, Published online 2024.

91. I. Zarazua, G. Han, P. P. Boix, et al., "Surface Recombination and Collection Efficiency in Perovskite Solar Cells From Impedance Analysis," *Journal of Physical Chemistry Letters* 7, no. 24 (2016): 5105–5113, https://doi.org/10.1021/acs.jpclett.6b02193.

92. I. Zarazúa, S. Sidhik, T. Lopéz-Luke, et al., "Operating Mechanisms of Mesoscopic Perovskite Solar Cells Through Impedance Spectroscopy and J-V Modeling," *Journal of Physical Chemistry Letters* 8, no. 24 (2017): 6073–6079, https://doi.org/10.1021/acs.jpclett.7b02848.

93. O. Almora, K. T. Cho, S. Aghazada, et al., "Discerning Recombination Mechanisms and Ideality Factors Through Impedance Analysis of High-Efficiency Perovskite Solar Cells," *Nano Energy* 48 (2018): 63–72, https://doi.org/10.1016/j.nanoen.2018.03.042.

94. L. Contreras-Bernal, S. Ramos-Terrón, A. Riquelme, et al., "Impedance Analysis of Perovskite Solar Cells: A Case Study," *Journal of Materials Chemistry A Materials* 7, no. 19 (2019): 12191–12200, https://doi.org/10.1039/c9ta02808k.

Supporting Information

Additional supporting information can be found online in the Supporting Information section.